technologies

MDPI

Article

Hybrid Cavitation-Jet and Arc Discharge Technology for Processing Associated Petroleum Gas

Galymzhan Mamytbekov [1], Igor Danko [1,2,*], Amangeldy Bekbayev [2], Vassiliy Titkov [3] and Yernat Nurtazin [1]

[1] Institute of Nuclear Physics, Almaty 050032, Kazakhstan; g.mamytbekov@inp.kz (G.M.); nurtazin@inp.kz (Y.N.)
[2] Department of Power Engineering, Satbayev University, Almaty 050013, Kazakhstan; a.bekbayev@satbayev.university
[3] Institute of Energy, Peter the Great St. Petersburg Polytechnic University, Saint Petersburg 195251, Russia; titkov_vv@spbstu.ru
* Correspondence: i.danko@inp.kz

Abstract

This study investigates the feasibility of treating acidic gases produced in oilfields using a novel method that combines cavitation-jet reactor (CJR) technology with electric arc discharge (EAD). The integration of these two approaches enhances the ionization process by converting neutral gas molecules into chemically reactive ion-radical and radical fragments. These highly reactive species eventually recombine, creating new chemical compounds and simpler molecules from incoming acid gas and water vapor. Theoretical validation and experimental demonstration have revealed possible mechanisms and pathways of low-temperature plasma-chemical processes resulting from the synergistic effects of cavitating-jet flow and arc discharge on the molecular degradation of neutral gaseous molecules, such as hydrogen sulfide and carbon dioxide in water vapor, which lead to the generation of new compounds. Research indicates that the most effective method for processing associated petroleum gas (APG) involves minimizing the sequential nature of chemical reactions in low-temperature non-equilibrium plasma environments, thus eliminating the need for costly and complex catalysts. Additionally, studies have shown that the cavitation-jet flow of a gas–vapor–liquid mixture, when combined with an electric arc discharge in the truncated region of the low-temperature plasma of CJR, results in the synthesis of hydrogen, two forms of S_8 (S_8^{I} and S_8^{II}), crystalline carbon, and its organic derivatives containing oxygen and nitrogen, specifically methanol, ethanol, acetone, and acetonitrile. The data obtained suggest that the generation of low-temperature plasma in the cavitation-jet chamber, induced by an electric discharge, is essential for the production of reaction products, such as hydrogen, sulfur, and oxygen- and nitrogen-containing derivatives of organic carbon, when water vapor and acid gas molecules traverse the reactor.

Keywords: hybrid plasma technology; low-temperature plasma; plasma-chemical processing; associated petroleum gas processing; reforming of methane; hydrodynamic cavitation; hydrogen generation

Check for updates

Academic Editor: Christos A. Aggelopoulos

Received: 17 February 2026
Revised: 5 March 2026
Accepted: 9 March 2026
Published: 12 March 2026

Copyright: © 2026 by the authors. Licensee MDPI, Basel, Switzerland. This article is an open access article distributed under the terms and conditions of the Creative Commons Attribution (CC BY) license.

1. Introduction

Associated petroleum gas (APG) serves as a significant natural resource, utilized as both fuel and a raw material for chemical production, thereby influencing the resolution of social and economic challenges in nations primarily involved in oil and gas extraction [1].

In some countries, particularly Kazakhstan, there is a notable discrepancy between oil production rates and the development of infrastructure needed to efficiently utilize associated petroleum gas. As a result, oil companies have resorted to the on-site incineration of significant amounts of this valuable petrochemical and energy resource [2]. This practice leads to the waste of important chemical and energy resources and causes considerable environmental damage to the surrounding biosphere, transforming this issue from a local and national concern into a matter of global importance. The combustion products from associated petroleum gas play a significant role in increasing greenhouse gas emissions, with the annual global volume of APG burned reaching hundreds of billions of cubic meters [3,4].

Currently, researchers are concentrating on alternative energy, which encompasses a range of promising techniques for acquiring, storing, transporting, and utilizing energy from renewable sources that are less prevalent than conventional ways. Furthermore, in numerous instances, alternative energy sources are better localized and, when combined with conventional energy resources, enhance energy security [5–7].

Low-temperature plasma is a state of matter characterized by the generation of ionized gases (plasma) at reduced temperatures, facilitated by ionizing radiation, electrical discharges, or cavitation flows of liquids or gases through tubes of certain cross-sections [8–10]. Low-temperature plasma technology (LTP) is energy-efficient, non-toxic, and generates no waste, rendering it an environmentally sustainable alternative to conventional manufacturing processes, such as hydrogen [10–18].

Today, innovative models and methodologies are being developed to enhance the design of equipment for executing high-temperature chemical processes, utilizing advanced technological solutions focused on minimizing the energy and material intensity of primary equipment. From this perspective, the most effective strategy is to perform multi-stage chemical processes under non-equilibrium plasma conditions at moderate temperatures, ideally without utilizing costly and intricate catalysts composed of non-ferrous and platinum group metals [19–21].

Non-equilibrium plasma has notable applications in the purification of gas emissions from industrial sources and vehicles, effectively removing organic substances, nitrogen oxides, and soot. The mechanism for stimulating redox reactions in gas flows excited by electric discharge is elucidated through the heating of electronic and vibrational degrees of freedom of gas molecules. This process leads to the formation of $OH^{\bullet}$, $O^{\bullet}$, $N^{\bullet}$, and $H^{\bullet}$ radicals, which enhance the chemical processes in the purified gas. The purification level attained in this process can surpass 99% while maintaining relatively low electrical energy consumption [20–23].

The proposed article aims to utilize associated gases containing hydrogen sulfide by applying advanced cavitation technology to create conditions favorable for the generation of low-temperature non-equilibrium plasma (LTP).

To achieve this goal, a cavitation-jet reactor (CJR) is employed, which includes a cavitation-jet chamber (CJC) capable of producing a substantial number of ionized active particles and radicals [24,25]. An electric arc discharge was utilized as an additional source of ionization for the vapor–gas mixture, as it generates intense radiation across a broad spectrum of wavelengths when ignited in air. Approximately 70% of radiation energy is found in the ultraviolet range, 15% in the visible range, and 15% in the infrared range [9,10].

Notably, there is currently a dearth of comprehensive information about these kinds of studies in technical and scientific publications. The collected data, which might be either qualitative or semi-quantitative, are analyzed in this work. We have previously shown that numerical modeling tools for mechanochemical reactions can be used to understand the quantitative features of the processes that take place during the cavitation-jet treatment of a

gas–vapor–liquid combination in the CJ reactor. These processes facilitate the recombination of newly generated ions and radical particles obtained during the cavitation-jet treatment of the water–gas mixture, leading to the formation of new compounds.

2. Materials and Methods

2.1. The Principle of Operation of the Cavitation-Jet Reactor

The schematic diagram of the CJR with an electric arc discharge is presented in Figure 1. Distilled (desalinated) water (Figure 1, pos. 1) is pumped by the PQ 3000-MF pump (Pedrollo S.p.A., San Bonifacio (VR) Iraly), with a maximum flow rate of 50 L per minute and a maximum pressure of 18 bar (Figure 1, pos. 2), into the cavitation-jet chamber, which consists of three main sections (Figure 1, pos. 3, 4, 7). The first section (Figure 2a) is a Venturi tube (VT) equipped with a rotating flow activator-vortex generator, designed in the form of a screw with external grooves and an internal through channel. The function of the flow activator is to divide the incoming stream of pressurized liquid from the centrifugal pump along its outer and inner contours. Both along the external (helical grooves) and the internal contour (through channel with a diameter of 3 mm), the flow of liquid accelerates according to the laws of aerodynamics. It should be noted that the separated turbulent flows have different velocities as they pass through the Venturi tube activator, and consequently, they will be characterized by different amplitude-frequency parameters, leading to the formation of cavitation bubble inception zones.

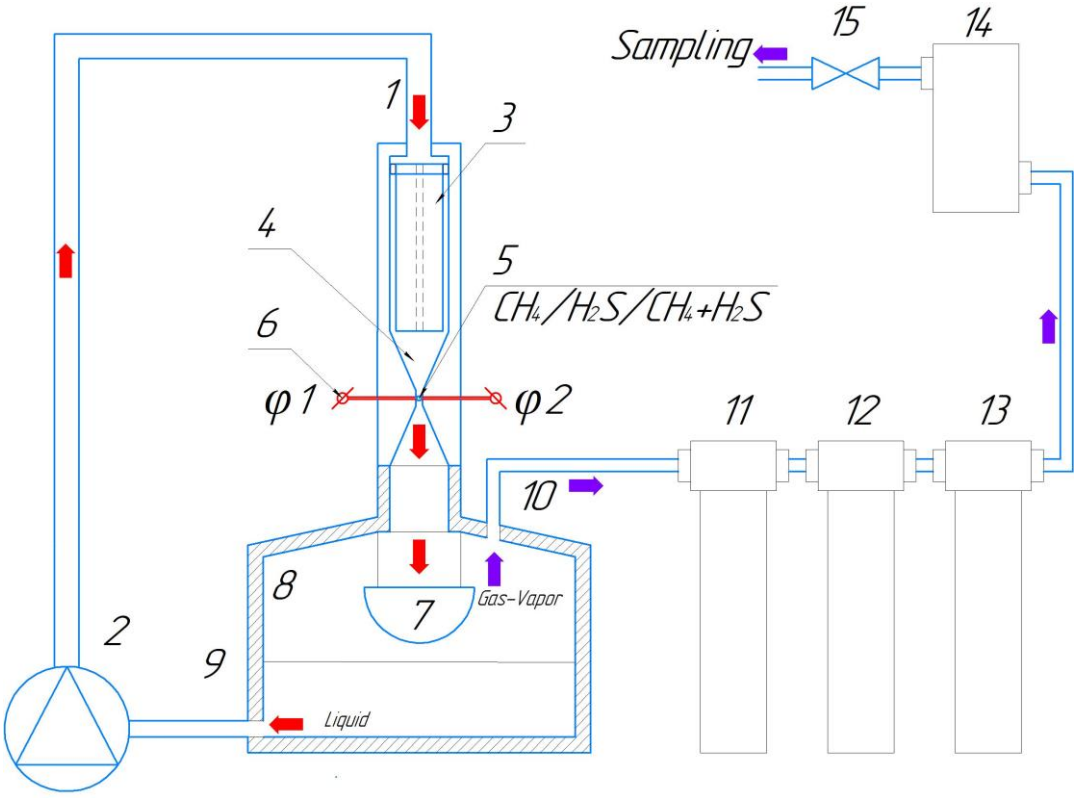

Figure 1. Diagram of the experiment using a hydrodynamic cavitation-jet reactor: (1) water supply to the cavitation-jet reactor; (2) pump with a capacity of 50 L/min and a maximum pressure of 18 bar; (3) Venturi tube with a rotating mechanism; (4) Laval nozzle; (5) gas supply nozzle; (6) electrodes for medium ionization (3–20 kV, 1–2000 Hz, 200 W); (7) cavitation-jet flow reflector; (8) hydrodynamic cavitation-jet reactor chamber; (9) channel for circulating steam–gas mixture; (10) channel for collecting heated gas mixture; (11) flow cooler; (12) silica gel dryer; (13) carbon filter; (14) nitrogen trap; (15) valve. Red arrows indicate the direction of movement of the gas-liquid phase. Blue arrows indicate the direction of the vapor-gas phase.

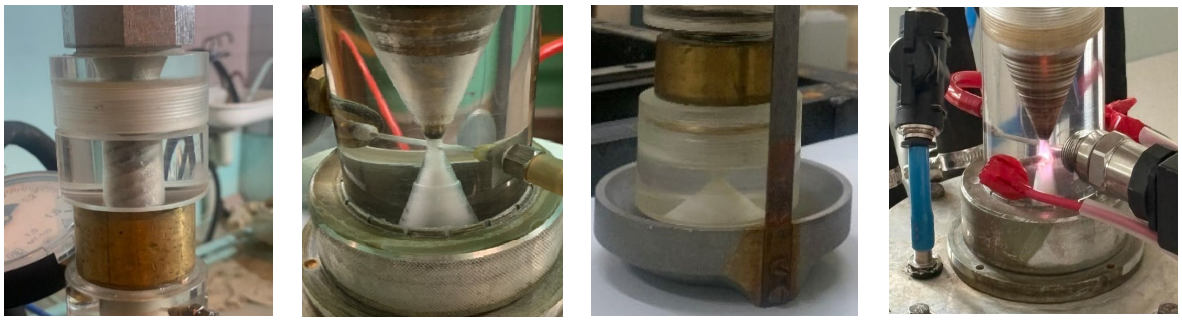

(**a**) (**b**) (**c**) (**d**)

Figure 2. Main structural elements of the cavitation-jet chamber: (**a**) Section 1—Venturi tube with rotating actuator; (**b**) Section 2—Laval nozzle; (**c**) Section 3—cavitation-jet flow reflector; (**d**) Section 4—electric arc formation zone.

A combined pressure sensor installed perpendicular to the electrodes (position 6, Figure 1) was used to measure pressure in various zones of the cavitation-jet chamber. This sensor quantifies pressure relative to atmospheric pressure, accommodating both vacuum conditions (below atmospheric pressure) and overpressure conditions (above atmospheric pressure). A detailed diagram of the information-measuring system of the cavitation-jet reactor and the characteristics of the sensors used are presented in the work [26].

A white region with vapor–gas cavitation is observed in the area of maximal liquid expansion in the Laval nozzle (LN) (Figure 2b). This can result in modifications to the technological parameters of fluid flow, particularly in narrow dielectric CJR channels, for the multi-bubble cavitation regime.

A high-voltage alternating current power supply (pulse modulator) was employed to generate and sustain an electric arc within the Laval nozzle, facilitating enhanced ionization of the vapor–gas mixture. This device allows for the adjustment of output voltage, pulse repetition frequency, cycle duration, and control frequency.

The voltage from the high-voltage AC power supply was applied to brass electrodes (Figure 1, pos. 6). The electrodes have the ability for screw adjustment to change and regulate the arc length.

Table 1 shows the nominal parameters of the high-voltage power supply, including the output voltage range from 3 to 20 kV used to supply voltage to the electrodes (Position 6, Figure 1) for ionization of the medium. The arc ignition and burning voltage is related to the ionization potential of the medium in which ignition occurs. In the hydrodynamic cavitation-jet reactor used, demineralized water with a high resistance to alternating current was used as the working fluid (medium). The arc ignition is carried out without touching the electrodes; therefore, the ignition voltage differs significantly from the arc burning voltage. Thus, a voltage of up to 20 kV was used to ignite the arc; after arc ignition, the arc voltage decreased to 4.24 to 4.32 kV. Arc burning was maintained at a voltage in the range from 4.24 to 4.32 kV at a pulse frequency of 2000 Hz.

Table 1. Nominal parameters of the high-voltage alternating current source.

Parameters	Value/Range	Unit/Notes
Input voltage (AC)	180–250	V
Input voltage frequency	50	Hz
Output voltage (AC)	3–20	kV
Output current	0–10	mA
Pulse repetition frequency	1–2000	Hz
Max output power	200	W

Simultaneously, the application of a high potential difference (ranging from 3 to 20 kV) to the electrodes (refer to Figure 1, pos. 6) in the region of maximum constriction of the Laval nozzle (see Figure 1, pos. 5) results in further ionization of the gas–vapor–liquid (GVL) mixture. The ionized vapor–gas mixture flows into the chamber of the hydrodynamic cavitation-jet reactor (Figure 1, pos. 8). The resulting heated gas mixture is directed through channel (Figure 1, pos. 10) for subsequent separation. The gas mixture is routed to a flow cooler (Figure 1, pos. 11), where it is cooled through a heat exchanger by a counterflow of water. The cooled mixture is directed to unit (Figure 1, pos. 12) for the removal of water vapor utilizing silica gel. The pre-dried gas mixture undergoes filtration through a carbon filter (Figure 1, pos. 13). The nitrogen trap (Figure 1, pos. 14) serves to decrease the partial pressure of the gas mixture and to condense residual vapors by freezing them out. The dehydrated vapor–gas mixture is collected in the oxygen cushion (OC) through a ball pneumatic valve (Figure 1, pos. 15).

The upper cover in the design of the CJR facilitates possibilities in which the vapor can be regarded as saturated in relation to the specified temperature and pressure. The operating modes of the cavitation-jet chamber and the discharge device regulate the temperature of the solution. In the single pulse mode, the vapor density is influenced by the external temperature. Conversely, in the frequency or continuous mode, significant heating and evaporation occurs as a result of the solution being heated by the discharge current itself.

2.2. XRD Analysis

An X-ray diffraction analysis (XRD) was provided using a Bruker X-ray diffractometer (Billerica, MA, USA), employing CuKα radiation as the source. The dry powder, sized up to 10 μm, was produced through an experiment involving cavitation-jet action during an electric arc discharge. It was scanned withing a range of 2θ angles from 20° to 70°, with a step of 0.02°, a scanning speed of 2 s/point, and radiation parameters set at 40 kV and 40 mA.

2.3. Scanning Electron Microscopy

A Hitachi model TM 4000 Plus microscope (Tokyo, Japan) equipped with an X-ray fluorescence energy dispersive analysis (EDS) attachment and a crystal detector was used to perform scanning electron microscopy (SEM). The samples were examined in the backscattered electron mode at low vacuum.

2.4. Gas Chromatographic Analysis

The Agilent 7890A gas chromatograph (Wilmington, DE, USA) was utilized for the identification and quantitative determination of volatile organic compounds in the mixture. The information gathered throughout the examination is processed utilizing MSD Productivity ChemStation software (G1701EA E.02.00).

The approach facilitates the precise separation and identification of the mixture's components. A water-cooled trap effectively minimizes the background signal, thereby enhancing sensitivity. Peak identification was conducted by analyzing the retention time of the compounds in capillary columns, resulting in a report that utilized the percentage normalization method for quantitative analysis and identification.

2.5. Determination of the Gases in Vapor–Gas Mixture

The gas content in the vapor–gas mixture was determined using the portable multichannel gas detector TOP-SENS 610 ("TOP-SENS" LLC, Moscow, Russia). The measurement ranges were methane—0–100 vol.%, hydrogen, H_2—0–1000 ppm, hydrogen sulfide, H_2S—0–100 ppm, carbon monoxide, CO—0–1000 ppm, and oxygen, O_2 0–30 vol.%.

The analysis was conducted using an RGA-100 gas analyzer (Stanford Research Systems, Sunnyvale, CA, USA) for mass spectrometry, capable of detecting gases within a mass range of 1 to 100 a.m.u. The plant is equipped with a high-vacuum Agilent TPS Flexy-304FS pumping station (Tokyo, Japan), which is based on a Turbo-V 304-FS turbomolecular pump and a dry spiral pump IDP-7 (Tokyo, Japan) from Agilent Technologies (Tokyo, Japan). The gas detection principle involves ionizing a fraction of the gas molecules, sorting the resulting positive ions by mass, and measuring them. The detection device used is a Faraday cylinder.

Determination of gas composition was carried out using a stand designed for the analysis of the mass spectrum of residual gases (refer to Figure 3).

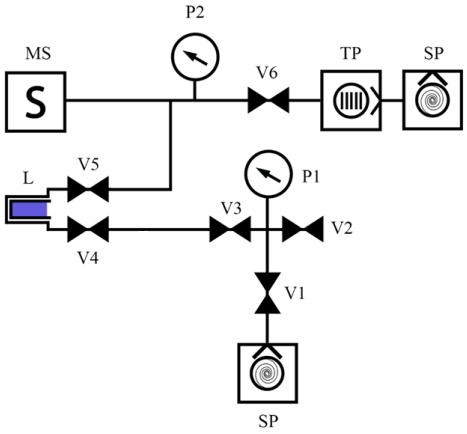

Figure 3. Schematic diagram of the mass spectrum analysis stand for residual gases: MS—quadrupole mass spectrometer, TP—turbomolecular pump, SP—spiral (forevacuum) pump, L—nitrogen trap, P1—vacuum pressure sensor of the experimental device, P2—vacuum pressure sensor in the mass spectrometer chamber, V—vacuum valves.

The mass spectrometer (Figure 3, MS) chamber is evacuated to a high vacuum of ~1.6×10^{-7} mbar, and background readings are then taken. The sample gas cushion is connected to valve (Figure 3, V2), and the section from valve (Figure 3, V2) to valve (Figure 3, V5) is evacuated to a medium vacuum of ~2×10^{-2} mbar using a scroll pump (Figure 3, SP). The pump valve (Figure 3, V1) is then closed. Gas is then released from the sample gas cushion using vacuum valves (Figure 3, V2, V3, V4, and V5). The gas composition is analyzed using an RGA-100 residual gas analyzer (Stanford Research) (Figure 3, MS).

3. Results and Discussion

The mathematical model for the steam conversion of methane, as developed in references [24,25] using the COMSOL 5.6 Multiphysics simulation software, allowed the calculation of essential process parameters. These include the concentrations of methane, hydrogen, carbon monoxide, and carbon dioxide, as well as the temperature variation along the length of the cavitation-jet reactor chamber. The model effectively describes the chemical interactions among the components and considers the impact of operational conditions, such as temperature, pressure, and steam/gas ratio, on process efficiency.

The introduction highlights that effectively utilizing produced associated petroleum gas (APG) is a critical challenge in energy and resource conservation. To mitigate air pollution caused by harmful substance emissions and to decrease greenhouse gas emissions produced during the combustion of associated petroleum gas, low-temperature plasma-chemical processes are extensively utilized [27–30]. In contrast to conventional high-temperature plasma, low-temperature or nonthermal plasma [24] can be generated at room temperature, enhancing its safety and versatility for various applications. An ap-

proach to extracting hydrogen from hydrocarbon-containing feedstock involves leveraging the catalytic activity of non-equilibrium low-temperature plasma in chemical reactions. The development of plasma-catalytic reactors has resulted in significant gains, including elevated specific productivity and improved environmental cleanliness.

The energetic equivalent of thermodynamic temperature in the context of a glow discharge can be expressed as follows: the translational and rotational degrees of freedom of gas molecules, with an average energy of around 0.03 eV, correspond closely to room temperature [20]. Simultaneously, the vibrational degrees of freedom possess an average energy of approximately 0.3 eV, which in an equilibrium context would equate to a temperature of several thousand degrees. Furthermore, the electronic degrees of freedom are defined by an average energy of several electron volts, which, under equilibrium conditions, would correspond to a temperature of several tens of thousands of degrees. The preservation of a non-equilibrium state in the gas is feasible solely due to an external electric field, which energizes the electrons in the discharge, providing sufficient energy for gas ionization and conductivity, as well as for the excitation of the internal degrees of freedom of the atoms and molecules of the working gas. The intensity of the non-equilibrium activity must significantly exceed that of the equilibrium process given identical energy input into the plasma [31].

3.1. Tests of a Cavitation-Jet Reactor with an Electric Arc Discharge

Chemically active plasma (CAP) is of significant interest to researchers due to its capability to facilitate selective chemical reactions at exceptionally high velocities. Simultaneously, varying plasma parameters enable the regulation of chemical processes, steering them toward the intended outcomes and enhancing their energy efficiency.

The study [20] provides an analysis of the kinetics of plasma-chemical processes, highlighting that the most energy-efficient processes are those that selectively occur through vibrationally excited states of molecules. These states are marked by a significant difference between vibrational temperature and translational temperature. Such processes are most effectively carried out in gases that are highly vibrationally agitated and have relatively slow relaxation, including N_2, CO, and CO_2.

The energy efficiency of plasma-chemical reactions driven by molecular vibrational excitation is highly influenced by the conditions of the discharge. The optimal efficiency is attained within a limited spectrum of plasma parameters. The electron temperature should be sustained at approximately 1 eV, significantly surpassing the translational temperature (T_0 < 103 K). The ionization degree must not be less than 10^{-7}–10^{-6}. This rule is much stricter when it comes to breaking down water. Achieving these precise conditions requires meticulous control over various factors, including gas flow rates and discharge power. Additionally, the specific energy input required is 1 eV/mol (around 5 J/cm^3 atm) [20,31].

An arc discharge in water vapor can generate low-temperature plasma due to the arc's elevated temperature, leading to combustion within the water vapor, which has a diameter nearly equivalent to that of the arc. The voltage of the arc during burning in water vapor is 1.3 to 1.35 times greater than in air. The average electric field strength measured along the arc's length in the vapor was 18–20 V/cm [31].

Upon interacting with water, plasma primarily produces hydroxyl radicals ($OH^{\bullet}$) through both chemical and physical mechanisms [32]. The excited particles and electrons within the plasma provide the energy needed to break the chemical bonds of H–OH, resulting in the generation of these radicals.

The electrode temperature in our cavitation-jet reactor corresponds to the temperature of the gas–vapor–liquid (GVL) mixture flow at the throat zone of the Laval nozzle. Here, the GVL undergoes maximum atomization and forms a cavitation cloud. A steady discharge

electric arc with bright luminescence is partially generated by this rarefied medium. At low temperatures, ranging from room temperature to 40 °C, the color of the arc shifts from bright red to bright violet. This shift continues between 60 and 90 °C (Figure 2d).

Previous studies [24,25] demonstrated that hydrogen generation occurs during cavitation-jet flow in the apparatus investigated in this research. Significant hydrogen production, along with increased levels of methane and carbon monoxide, has been observed within the temperature range of 60 °C to 80 °C. This was detected through gas chromatography–mass spectrometry analysis and measured using a concentration sensor for the specified gases at the outlet of the reaction zone.

The cavitation theory posits that the region linked to the creation of vapor–gas cavities within the liquid initiates when the local absolute pressure in the completely degassed liquid decreases to the level of the saturated vapor pressure [33]. However, in a real liquid, this process starts earlier due to the presence of cavitation nuclei created by dissolved gas molecules such as oxygen, nitrogen, and carbon dioxide (CO_2). In a closed chamber with solid walls, the initial phase of vapor–gas cavity formation may commence sooner because the liquid can detach from the solid wall of the VT activator if the adhesion force of the liquid on the wall is less than the absolute pressure within the liquid. Additionally, active cavitation nuclei can form on the solid wall of the centrifugal pump impeller, which has a partially hydrophilic surface, as well as on the dielectric surface of the cavitation-jet chamber casing.

Three zones of pressure drop were conditionally analyzed, resulting in the formation of a cavitating-jet flow regime for a gas–vapor–liquid mixture, which can be regarded as low-temperature plasma [34,35].

The binary cavitation flow that originates from the Venturi tube evolves into a Laval nozzle when the tensile stress within the liquid exceeds its tensile strength threshold, which can lead to vapor cavitation. It is crucial to note that while a reduction of 1–2% in the local pressure of the liquid is sufficient for gas cavitation to occur, a much more significant decrease in pressure—by several orders of magnitude—is necessary to initiate vapor cavitation, ultimately reaching the saturation vapor pressure of the liquid itself [10,11].

The initial pressure (P1, Figure 4a) originates from the impeller of the centrifugal pump and is determined by the pump's liquid delivery parameters, corresponding to a value of 15 atm. The second pressure sensor is positioned in the narrow section of the Laval nozzle, where the liquid flow experiences maximum rarefaction, transitioning into a gaseous or vapor state. At this point, the pressure of the liquid–gas mixture (LGM) flow takes on a negative value (P2, Figure 4b). The third pressure value (P3, Figure 4c) reflects the pressure of the fluid–gas mixture at the outlet of the Laval nozzle's convergent section as it enters the free volume of the circulation container. While pressures P1 and P2 remain relatively stable, P3 displays significant fluctuations, oscillating between positive and negative values. This variation indicates complex processes involving the appearance and disappearance of new bubbles, particularly their merging to form new vapor–gas phases with different volumes. Ultimately, these processes lead to a transition into liquid due to the condensation and merging of droplets within the vapor–gas mixture.

As the bubbles collapse, a noticeable increase in pressure and temperature occurs at the outlet of the Laval nozzle, indicating an elevation in the internal energy of the system. An aluminum reflector was positioned above the level of the circulating fluid to enhance the collapse effect and facilitate further atomization of the cavitating bubbles in the working fluid, located 10 cm from the Laval nozzle (see Figure 1, position 7, and Figure 2c). The interaction among bubbles reduces their expansion while simultaneously intensifying their collapse. This interaction results in a delay in the time required for the bubbles to reach their maximum and minimum radii. The accumulation of energy within each bubble

logically increases as the number of neighboring bubbles grows. This behavior stems from various factors, including changes in local sound speed, increases in temperature, pressure variations, and the duration of bubble expansion and collapse, as well as the presence of electric double layer at the interphase boundary of the bubble-vapor or bubble-liquid [36]. Two succinct explanations for this phenomenon are derived from numerical results: the collapse force of the inner bubble is intensified by pressure impulses generated by the early collapse of outer bubbles impacting the inner bubble [37] and by the absorption of energy from the surrounding liquid to maintain its oscillation. As the bubble reaches its minimum size, the internal energy within it escalates to its peak, resulting in the emission of pressure impulses outward. This observation is particularly evident in the temperature change profile over time (see Figure 4d,e).

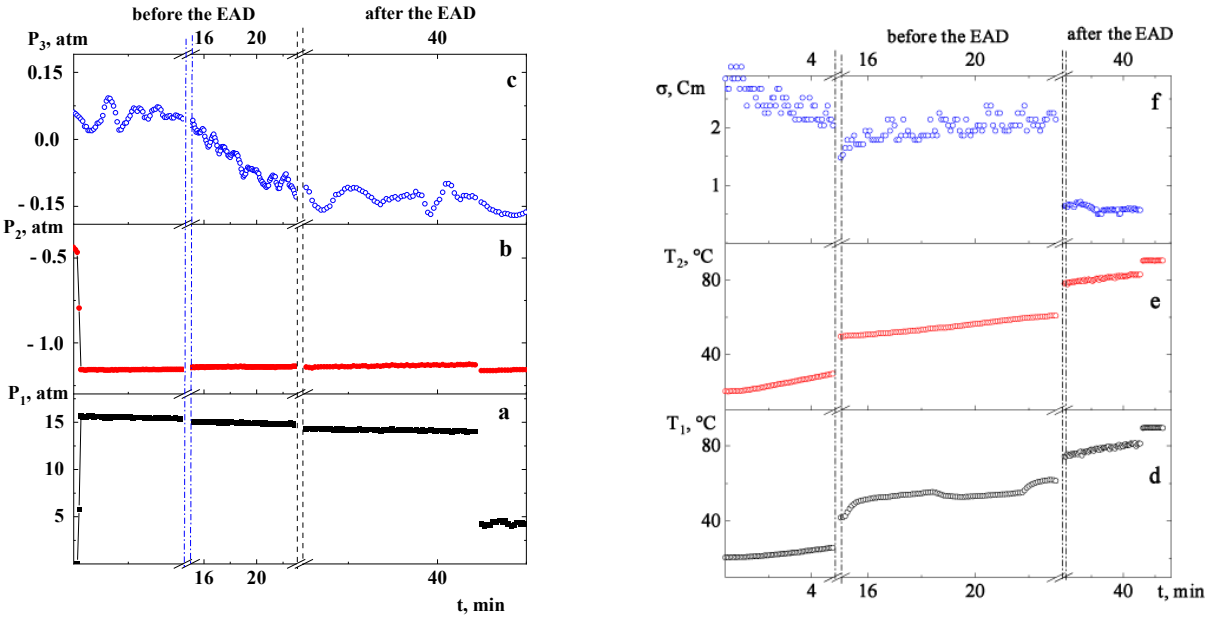

Figure 4. Change in pressure across the flow zones of the vapor–gas–liquid in the cavitation-jet reactor (**a**–**c**), temperature (**d**,**e**), and conductivity (**f**) over processing time.

The temperature of the working fluid circulating within the cavitation-jet reactor increased significantly in the absence of an electric arc, and this increase occurred almost linearly over time [25]. The presence of an electric arc within the cavitation zone leads to a sudden change in temperature. An electric arc was generated at the 15 min mark after the centrifugal pump was initiated, coinciding with the liquid temperature reaching 35 °C. Following this, a notable temperature rise was observed in both the circulating liquid and the vapor in the free zone of the container, with the vapor temperature increasing by 2–3 °C before the liquid temperature began to rise. During the 15 min of electric discharge, a steady increase in the temperature and electrical conductivity (Figure 4f) of the liquid phase was recorded. This increase may be associated with the production of charged particles—such as proton and hydronium ions, hydrogen, oxygen, and OH radicals—resulting from the molecular breakdown of water molecules. Consequently, the simultaneous generation of low-temperature plasma due to liquid cavitation, combined with energy absorption from the electric arc of cavitating bubbles, creates a synergistic effect. This effect promotes the formation and accumulation of active particles (radicals, ions, and ion-radicals), which can undergo further chemical transformations, ultimately leading to the formation of new compounds not present in the original working fluid (water).

The mechanism of ionization of the neutral molecules within the vapor–gas phase in a low-pressure zone, influenced by an electric arc discharge, resembles the radiolysis of

water caused by high-energy radiation, including electron beams, γ-radiation, or ultrasonic exposure [38,39].

$$H_2O \xrightarrow{\text{water radiolysis}} e_{aq}^{-}, \dot{H}, H\dot{O}, H_2, O^{2-}, H_2O_2 \quad (1)$$

Frenkel's theory suggests [40] that cavitation bubbles in water form like small droplets within a solid medium, generating significant charges of opposite signs, similar to the way ionic crystals split apart. Subsequently, electrical discharges occur between the walls of the cavitation bubbles within the vapor–gas medium, resulting in the excitation of gas molecules and atoms.

The cavitation-jet flow of the vapor–gas mixture generates weakly ionized plasma, which results in the formation of intermediate active particles, including hydroxyl radicals ($HO^{\bullet}$), hydroperoxyl radicals ($HO_2^{\bullet}$), atomic hydrogen ($H^{\bullet}$), and atomic oxygen ($O^{\bullet}$). Additionally, the release of weakly ionized plasma promotes the production of hydrogen peroxide (H_2O_2) and superoxide anions (O^{2-}), which in turn contribute to the dissociation of water molecules.

Currently, when atmospheric air is supplied, there is a significant increase in the electric arc voltage from 4.2 V to 9.2 V, which is subsequently followed by a rapid decrease back to the initial breakdown value of 4.2 V once the air supply has stopped and the generation of hydrogen and carbon monoxide starts again.

Earlier, in the work [41], the emergence of supercritical water (SCW) in hydrodynamic cavitation devices was studied, and a conceptual model was proposed to explain the influence of bubble collapse dynamics on SCW formation. Supercritical water possesses unique physical properties compared to liquid water under ambient or subcritical conditions, including the weakening of hydrogen bonds between molecules, a lower dielectric constant of the medium, and high diffusion coefficients formed under these conditions of water exposure [42,43].

In model [41], the cavitation bubble is considered as a three-layer spherical system, consisting of gas inside the bubble, liquid outside the bubble, and a boundary layer of supercritical water. The results of the dynamic equation calculations indicate a negative impact of the supercritical water shell on the dynamics of cavitation bubble development. When the bubble collapses, the external fluid does positive work under the SCW shell and with the internal gas, raising their temperature, while the SCW shell receives a significant portion of the work. Therefore, during the collapse of the bubble, the kinetic energy is weak, and the temperature of the internal gas is relatively low due to the presence of the SCW shell. The SCW shell definitely slows down the oscillations of the bubble and cools the gas inside the bubble during its collapse, acting as a buffer absorption agent during bubble oscillations.

The studies on detecting OH radicals indicate that hydrodynamic cavitation acts as a low-frequency ultrasonic generator [38]. Optimizing chemical reactions during bubble oscillations can be accomplished by applying rapid restorative pressure in conjunction with a moderate bubble density.

At the outlet of the Laval nozzle diffuser, the total pressure along the axis of the cavitating jet gradually aligns with the equivalent static pressure in the chamber. Initially, the total pressure remains relatively stable; however, it experiences a significant decrease as it transitions into the free volume of the container (Figure 4c).

It is important to emphasize that for the consistent production of hydrogen and carbon monoxide (II), it is necessary to intermittently introduce atmospheric air into the system. This action was accomplished using an injector tube with a diameter of 2 mm, situated in the low-pressure zone of the Laval nozzle (Figure 2, pos. 5). The presence of dissolved gas molecules in the working fluid, specifically in water, which comprises components of air—primarily oxygen, nitrogen, and carbon dioxide—is crucial for the formation of

cavitation bubbles. These gases can affect the volatility of the solvent and serve as nuclei for the development of cavitation bubbles. Complete degassing of the solvent, caused by the increase in temperature, results in a decrease in the amounts of cavitation-generated gases H_2 and CO, as demonstrated by experimental observations.

Table 2 demonstrates that hydrodynamic cavitation occurring at temperatures between 30 and 35 °C can generate hydrogen, methane, and carbon monoxide (II) molecules. This suggests a radical mechanism for the degradation of water molecules, leading to the formation of $H^{\bullet}$ and $HO^{\bullet}$ radicals, as previously noted by the authors [39]. Additionally, thermodesorption spectroscopy data [25] confirms the presence of new molecules, including H_2, CO, and CH_4. The increase in temperature during hydrodynamic cavitation, due to the system's self-heating, accelerates the dissociation of water molecules into radicals or ion-radicals, thereby promoting the formation of new compounds. This process can be further enhanced by creating an electric arc discharge in the area of maximum gas pressure reduction, where a cavitation-jet flow of the working fluid is generated. This results in an additional increase in the temperature of the circulating working fluid and improves the yield of the desired product.

Table 2. Relative proportions of gas mixtures recorded by the gas sensor at different processing times [1].

Composition of Gases	Unit/Notes	CJT		EAD			CJT
		Total Processing Time, min					
		0	**5**	**15**	**20**	**35**	**50**
t, °C	°C	19	30	35	60	80	83
H_2	mg/m^3	0	17	25	46	90 [1]	72
CO	mg/m^3	0	42	77	203	503	373
CH_4	%LEL [2]	0	0	12	27	27	11
O_2	vol.%	19.4	19.4	19.4	21.2	20.9	19.4

[1] The detection limit of the gas sensor. [2] Low explosion level.

Some new compounds generated in the cavitation-jet reactor due to electric arc discharge are expected to exist in phases other than gaseous or vapor–gaseous forms. These compounds can be captured and separated during the operation of the cavitation-jet reactor. Furthermore, some of the newly formed compounds may migrate into the liquid phase when the vapor–gas mixture is cooled in a water-cooled receiver during the experiment or when the working fluid remains hot and is later cooled to room temperature.

The gas chromatography findings indicate the presence of novel carbon compounds containing nitrogen and oxygen within the condensed phase of the gas–vapor–liquid mixture, as illustrated in Table 3 and Figure 5. The potential for forming oxygenated derivatives of organic carbon during low-temperature plasma interactions involving water vapor and carbon oxides (CO and CO_2) is a topic of extensive research, supported by both theoretical computational mechanisms and experimental data [20,44–49]. Notably, the synthesis of acetonitrile is of particular significance, as it had not been previously detected nor expected to form [25,50].

The absence of methanol during sampling from the heated container occurs because, at this temperature, the alcohol molecules are either in a vapor state (boiling point MeOH = 64.7 °C; boiling point EtOH = 78.39 °C; boiling point acetone = 56.1 °C; boiling point CH_3CN = 81.6 °C) or have fallen below the detection threshold of the Agilent 7890A chromatograph (Wilmington, DE, USA).

Table 3. Data from gas chromatography of condensed phases of cavitation-jet water treatment under the influence of an electric arc [1].

Ret Time	Name of Product	Hot Container T = 80 °C	Cold Container T = 23 °C	Water Cooler T = 11 °C
		Amount [mg/mL]		
2.414	Acetone	2.74×10^{-5}	4.37×10^{-5}	3.02×10^{-4}
2.522	Methanol	-	1.30×10^{-4}	9.65×10^{-4}
2.642	Ethanol	9.96×10^{-5}	1.76×10^{-4}	1.44×10^{-4}
2.794	Acetonitrile	7.08×10^{-5}	-	7.98×10^{-4}

[1] Sampling corresponds to the temperature of the container and the refrigerator.

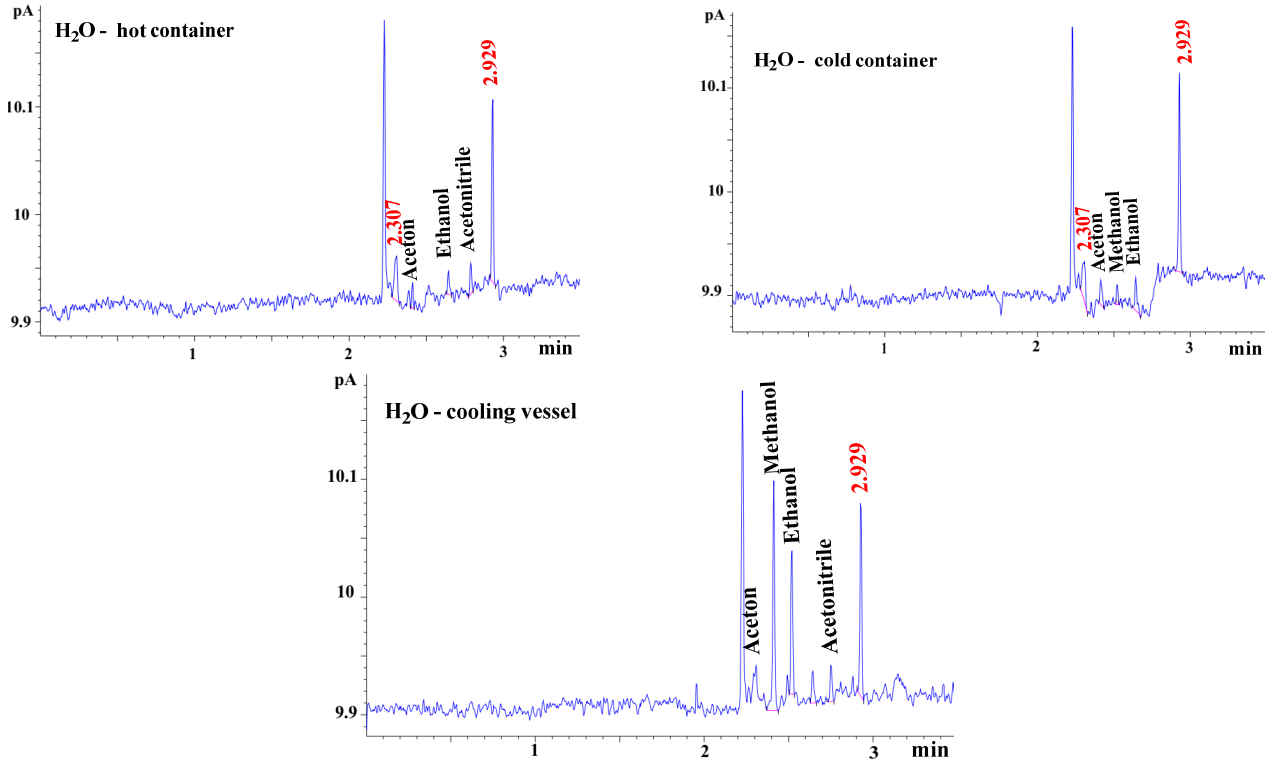

Figure 5. Gas chromatography data after cavitation-jet treatment in an electric arc discharge of distilled water.

Acetonitrile is produced industrially through the reaction of acetic acid with a slight excess of ammonia at temperatures ranging from 300 to 400 °C, using a γ-Al_2O_3 catalyst. This process yields the intermediate product acetamide. Additionally, acetic acid can be synthesized via the reaction between methanol and carbon monoxide, as shown in the scheme [50,51]:

$$CH_3OH + CO \rightarrow CH_3COOH \quad (2)$$

$$CH_3COOH + NH_3 \rightarrow CH_3CN + 2H_2O \; (\Delta G = -3.56 \frac{kJ}{mole}) \quad (3)$$

The conversion and selectivity of the reaction for producing acetonitrile from acetic acid and ammonia approaches 100% [52].

The only feasible method for ammonia formation may involve a gas-phase reaction between ionized water molecules and molecular nitrogen. This process occurs under low-temperature plasma conditions within a cavitation-jet reactor, influenced by an electric arc. The authors of studies on nitrogen [53,54] reached a similar conclusion, showing that water

droplets and nitrogen molecules can serve as feedstock in the plasma process for the sustainable and distributed production of ammonia or other nitrogen-containing compounds.

Equation (3) indicates the mechanisms for ammonia generation, which serves as a raw material for the production of acetonitrile, supported by evidence from the literature [53–55]:

$$N_2 \rightarrow 2\dot{N} \quad (4)$$

$$H_2O \rightarrow \dot{H} + O\dot{H} \quad (5)$$

$$\dot{N} + \dot{H} \rightarrow NH \quad (6)$$

$$NH + \dot{H} \rightarrow N\dot{H}_2 \quad (7)$$

$$N\dot{H}_2 + \dot{H} \rightarrow NH_3 \quad (8)$$

The initiation of chain formation may result from the dissociation of water molecules into $H^{\bullet}$ and $HO^{\bullet}$ radicals. However, the subsequent stages of ammonia formation through the reduction of the nitrogen radical by the same hydrogen radicals, which are produced from the plasma-chemical dissociation of water molecules in the cavitation zone of the CJR in the vapor phase, are entirely permissible.

This study illustrates that water molecules in vapor form within the cavitation zone of the reactor can function as H_2 molecules, serving as the primary raw material for the activation and fixation of N_2 in the plasma process. This method is environmentally friendly, safe, and easily accessible. The importance of hydrogen and carbon monoxide molecules, which result from the low-temperature plasma breakdown of water molecules and dissolved carbon dioxide leading to the formation of carbon monoxide (II), should not be underestimated. The mechanism of this process has been discussed in our previous studies [24,25,44].

Another important factor is the material composition of the structural elements of the cavitation-jet reactor (CJR), particularly the aluminum swirler used for the cavitating liquid. This swirler acts as both a catalyst and reagent, potentially serving as a source of hydrogen. The reasoning presented clarifies the mechanism and conditions under which acetonitrile is produced during the cavitation-jet treatment of water in the presence of atmospheric air, employing an electric discharge in the form of an electric arc within the cavitation-jet reactor.

3.2. Purification of Associated Petroleum Gas

A promising method for purifying associated petroleum gas from carbon dioxide and hydrogen sulfide involves preparing it directly in the field. However, for low-yield fields, traditional purification methods, such as the Klaus process and absorption techniques using alkanolamines, are often unprofitable and impractical. Absorption methods have several limitations, including high resource intensity, the need for corrosion inhibitors, low efficiency in amine utilization, slow reaction rates, the requirement for elevated temperatures, and the necessity for regenerating chemical reagents. Additionally, these methods generate waste gases, which require recycling measures or further disposal. Therefore, the development of compact and energy-efficient techniques for purifying natural gas from hydrogen sulfide and CO_2 is critically important [56,57].

Well-documented in the literature, the industrial technologies of the Fischer–Tropsch process [58] and the Haber–Bosch process [59,60] for producing hydrocarbon derivatives from syn-gas (H_2 + CO) and ammonia from a mixture (N_2 + H_2), respectively, occur at high temperatures (300–400 °C) and pressures (150–300 atm). Common to both processes is that hydrogen is obtained through multi-stage conversion of natural gas or gasification of coal, which also leads to energy consumption and the formation of greenhouse gases. However,

the organization of the technological cycle for producing oxygenated carbon derivatives in the first process and ammonia in the second process does not allow for the integration of these productions with hydrogen production technologies from renewable energy sources.

Since distilled water serves as the primary working fluid in low-temperature plasma processes, the overall changes in thermobaric parameters during high-pressure cavitating jet flow show a consistent profile across all examined examples (see Figure 4). It is important to evaluate the products of plasma-chemical processes that occur during cavitation-jet treatment in an electric arc discharge of a vapor–gas–liquid (GVL) mixture, which includes methane and hydrogen sulfide in both gaseous and condensed states.

3.2.1. System H_2O–CH_4

Table 4 presents the relative concentrations of gas mixtures measured by the gas sensor at various intervals during the cavitation-jet treatment (CJT) of distilled water, both with and without the application of an electric arc discharge. At the 20th minute of operation of the cavitation-jet reactor, injecting methane into the circulating liquid at a temperature of 60 °C leads to a significant decrease in the concentrations of CO, H_2, and molecular oxygen as the temperature increases to 83 °C. The expected reduction in the proportion of methane molecules occurs because they are directly involved in low-temperature plasma-chemical interactions with water molecules and the gases dissolved in them, particularly CO_2 and oxygen.

Table 4. Relative proportions of gas mixtures recorded by the gas sensor at different processing times (H_2O–CH_4) [1].

Composition of Gases	Unit/Notes	CJT		EAD			
		Total Processing Time, min					
		0	**10**	**15**	**20**	**35**	**50**
t, °C	°C	19°	30°	50°	60°	70°	83°
H_2	mg/m^3	0	18	27	32	29	16
CO	mg/m^3	0	79	141	167	131	89
CH_4	%LEL	0	0	14	100 [1,2]	84	62
O_2	vol.%	19.4	19.4	19.4	17.8	17.8	17.8

[1] The detection limit of the gas sensor. [2] Supply of methane from a gas cylinder.

The TDS analysis data (Table 5) further validate the observed trend of diminishing methane concentration in the steam–gas mixture, as well as molecular oxygen levels, during the hydrodynamic treatment (oxygen cushion No. 1, with sampling conducted prior to the nitrogen trap). When an electric arc discharge is applied to the cavitating-jet flow in the Laval nozzle, an increase in the concentration of gaseous H_2, N_2, and oxygen is observed (oxygen cushion No. 2, with sampling conducted after the nitrogen trap).

The mixture of neutral and partially ionized gases generated during the CJT undergoes further ionization upon interaction with electrons from the arc discharge. This process results in the formation of a sparkling electric arc discharge line (see Figure 2a) when the breakdown voltage is reached in the low-pressure region.

The increase in concentrations of nitrogen, oxygen, and argon molecules may be due to the periodic injection of atmospheric air into the CJC through a pipe in the Laval nozzle. This injection is essential for sustaining cavitation mode operation. Consequently, it enhances the number of cavitation nuclei, which are subsequently accelerated and collapse cumulatively.

Table 5. Relative proportions of gas mixtures recorded at different inflows into the TDS chamber [1].

Mass Number (M)	Possible Substances	The Source Is Entering the Mass Spectrometer Chamber	
		OC №1, % CJR	OC №2, % EAD
2	H_2	0.53	0.85
12	C_{12}	0.95	0.66
16	CH_4	73.46	53.45
18	H_2O	1.05	0.99
28	N_2	19.91	36.15
32	O_2	3.84	7.38
40	Ar	0.23	0.46
44	CO_2	0.03	0.06

[1] The gas composition was determined in the oxygen cylinder after the nitrogen trap at the outlet of the CJR.

The molecular destruction of water droplets due to the cavitation collapse of their bubbles (mechanolysis) alters the water structure, resulting in the formation of free hydrogen bonds and activated particles (radicals $H^{\bullet}$, $HO^{\bullet}$, and $H_2O^{\bullet}$). This process enhances their reactivity with neutral molecules of similar or different structures and compositions. Interactions result in the formation of new compounds, typically occurring under more extreme thermobaric conditions and with the use of catalysts [61].

$$H_2O \xrightarrow{\text{cavitation}} \dot{H} + \dot{O}H \qquad H_2O + e \xrightarrow{\text{electric arc}} \dot{H} + \dot{O}H \quad (9)$$

$$OH^- + H_2O_2 \rightarrow HO_2^{3-} + H_2O \qquad \dot{O}H + \dot{O}H \rightarrow H_2O_2 \quad (10)$$

$$OH^- + HO_2^{3-} \rightarrow H_2O + O_2 \qquad \dot{O}H + H_2O \rightarrow H_2O_2 + \dot{H} \quad (11)$$

The authors [62,63] previously demonstrated that the dissociation of an electronically excited hydrocarbon molecule, exemplified by methane, results in the generation of several particles. Each particle can be regarded as the initial stage in the formation of a new compound via a radical or ion-radical mechanism.

$$CH_4 + e \rightarrow \dot{C}H_3 + \dot{H}, \quad 76.0\% \quad (12)$$

$$CH_4 + e \rightarrow \dot{C}H_2 + H_2, \quad 14.4\% \quad (13)$$

$$CH_4 + e \rightarrow \dot{C}H + H_2 + \dot{H}, \quad 7.3\% \quad (14)$$

$$CH_4 + e \rightarrow C + 2H_2 \quad 2.3\% \quad (15)$$

The gas chromatography data of condensed phases (Table 6, Figure 6) further confirm the formation of new products during the low-temperature plasma-chemical process.

The sequence of reactions leading to the formation of the primary products identified in the condensed phase can be clarified through the following reactions:

$$\dot{C}H_3 + \dot{C}H_3 + CO \longrightarrow CH_3-\overset{\overset{O}{\|}}{C}-CH_3 \quad (16)$$

$$\dot{C}H_3 + \dot{C}H_2 + H_2O \rightarrow C_2H_5OH + \dot{H} \quad (17)$$

$$\dot{C}H_3 + H_2O \rightarrow CH_3OH + \dot{H} \quad (18)$$

$$\dot{H} + \dot{H} \rightarrow H_2 \quad (19)$$

Table 6. Data from gas chromatography of condensed phases of cavitation-jet water treatment under the influence of EAD.

Ret Time	Name of Product	Hot Container T = 80 °C	Cold Container T = 23 °C	Water Cooler T = 11 °C
		Amount [mg/mL]		
2.414	Acetone	4.49×10^{-5}	4.23×10^{-5}	2.74×10^{-4}
2.522	Methanol	5.92×10^{-4}	4.71×10^{-4}	5.33×10^{-4}
2.642	Ethanol	1.19×10^{-4}	-	8.97×10^{-5}
2.794	Acetonitrile	8.32×10^{-5}	2.73×10^{-5}	2.70×10^{-3}

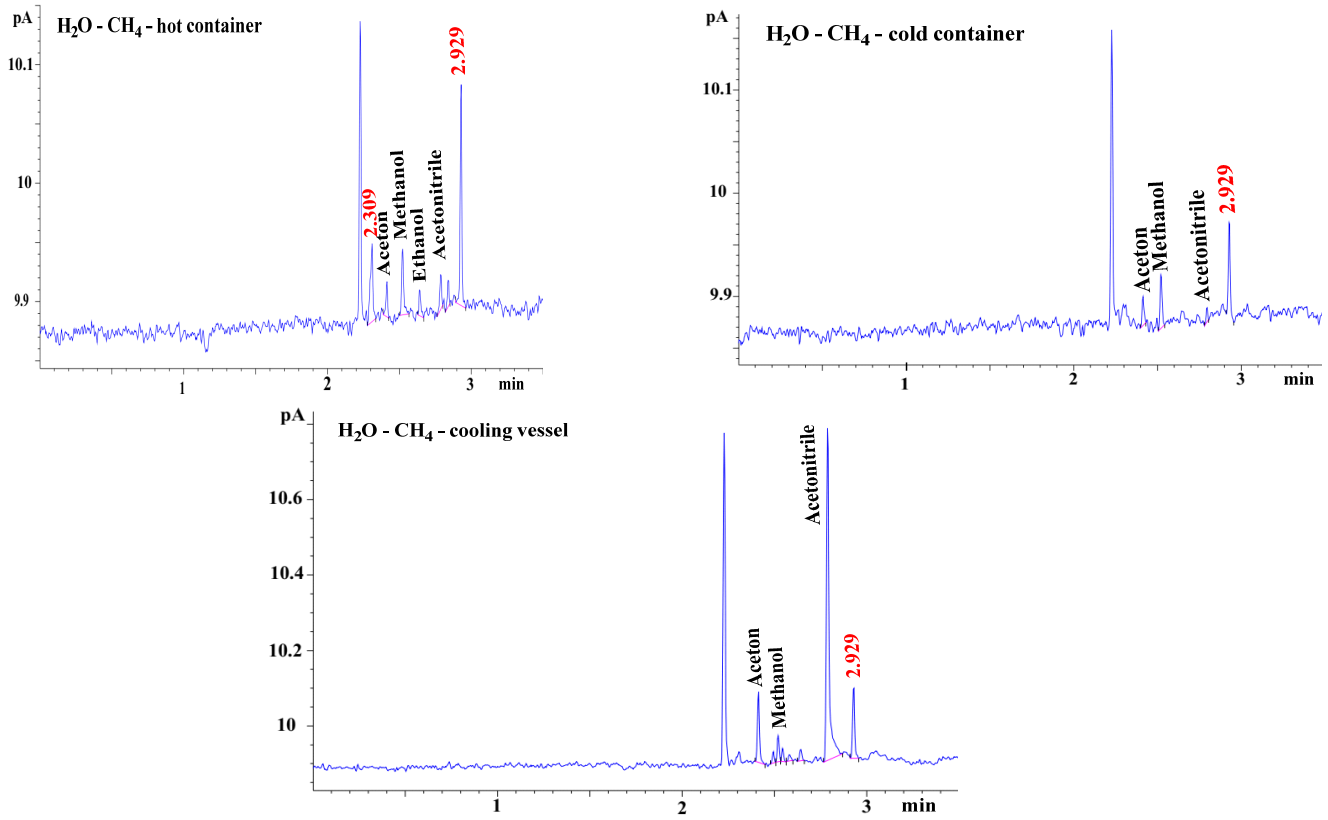

Figure 6. Gas chromatography data after cavitation-jet treatment in an EAD system of H_2O–CH_4.

The "death" of one radical resulting from a collision with another radical or a neutral water molecule is expected to result in the creation of a new compound along with one or more active radicals (such as $H^{\bullet}$, $OH^{\bullet}$, or $R^{\bullet}$). These radicals will eventually recombine to produce a new neutral molecule. The sequence of reactions that culminate in the generation of the primary products observed in the condensed phase can be elucidated through the subsequent reactions.

3.2.2. System H_2O–H_2S

Numerous studies focus on the dissociation of hydrogen sulfide in microwave discharge [64], alongside carbon dioxide [65], and in methane within barrier discharge [66]. This research seeks to develop methodologies for hydrogen generation and the extraction of elemental sulfur, which is an essential raw material in the chemical industry.

The bond dissociation energy of the hydrogen–sulfur bond in hydrogen sulfide is lower than that of the O-H bond in water and is comparable to the bond dissociation energy of the C-H bond in methane [64]. In a water molecule, the average O-H bond energy is

463 kJ, while in methane, it is 414.6 kJ, and in hydrogen sulfide, it is 389.1 kJ. Consequently, in terms of energy efficiency in thermal dissociation or electrolysis processes, hydrogen generation from hydrogen sulfide is more advantageous than from methane or water.

Table 7 illustrates the relative composition of gas mixtures measured by the gas sensor at various intervals during the cavitation-jet treatment of distilled water and electric arc discharge. At the 15th minute of the cavitation-jet reactor's operation, the introduction of hydrogen sulfide into the circulating liquid, along with reaching a temperature of 50 °C in the vapor–gas mixture, results in increased concentrations of CO, H_2, and CH_4. In contrast, the molecular oxygen content of the vapor–gas phase shows only a slight change. The reduction in the proportion of hydrogen sulfide molecules occurs naturally due to dissociation processes, which are affected by vapor–gas cavitation and the impacts of electric arc discharge on the vapor–gas–liquid flow within the Laval nozzle of the cavitation-jet reactor.

Table 7. Relative proportions of gas mixtures recorded by the gas sensor at different processing times (H_2O–H_2S) [1].

Composition of Gases	Unit/Notes	CJT		EAD	
		Total Processing Time, min			
		0	**15**	**25**	**50**
t, °C	°C	19°	50°	60°	83°
H_2	mg/m^3	0	16	21	90
CO	mg/m^3	0	75	98	68
CH_4	%LEL	0	0	19	24
H_2S	mg/m^3	0	152 [1,2]	65	33
O_2	vol.%	19.4	19.4	18.6	18.8

[1] The detection limit of the gas sensor; [2] supply of H_2S from the gas cylinder.

The data obtained from thermodesorption spectroscopy (Table 8) confirm the observed trend of decreasing hydrogen sulfide concentration in the vapor–gas mixture when the cavitating-jet flow is subjected to an electric arc discharge. There is an observed increase in the concentrations of gaseous H_2 and N_2, while free oxygen and sulfur dioxide are absent in quantities sufficient to draw definitive conclusions regarding their formation during the electric discharge.

Table 8. Relative proportions of gas mixtures recorded at different flow rates in the TDS mass spectrometer chamber.

Mass Number (M)	Possible Substances	The Source Is Entering the Mass Spectrometer Chamber
		Oxygen Cushion, % EAD
2	H_2	7.34
14	N [1]	5.94
28	N_2	81.98
32	H_2S	3.66
40	Ar	1.09

[1] The composition of the gas was determined in the oxygen cylinder after the nitrogen trap at the outlet of the CJR.

The final results of the gas mixture analysis, as shown in Tables 7 and 8, suggest a new pathway for developing the reaction mechanism of cavitating-jet flow influenced by an electric arc discharge:

$$2H_2S + CO_2 \rightarrow H_2 + H_2O + 2S^0 + CO \quad (20)$$

$$CO + H_2O \rightarrow CO_2 + H_2 \quad (21)$$

Based on the final results of the gas mixture analysis presented in Tables 7 and 8, we can propose a variant of the reaction pathway development occurring in the cavitation-jet flow under the influence of an electric arc discharge. There are alternative reaction pathways that may arise during an electric arc discharge. It is important to note that H_2S is highly soluble in water (2.6 L H_2S per 1 L H_2O at 20 °C). Thus, under low-pressure conditions in the cavitation-jet chamber, the cavitation bubble consists of spherical or elongated water droplets that contain hydrogen sulfide molecules. The collapse of these bubbles leads to the decomposition of the acid gas into hydrogen and elemental sulfur. Given that the bond energy of H-S-H is significantly lower than that of H-O-H, H_2S will primarily undergo molecular destruction in low-temperature plasma conditions. This phenomenon explains the noticeable increase in free hydrogen concentration, as indicated by gas sensors (Table 7) and TDS analysis (Table 8). Considering the results obtained in this study, the mechanism for the formation of these compounds can be represented by the following sets of reactions, which align well with the findings from works [64,65].

$$H_2S \xrightarrow{\text{cavitation}} H_2 + S^0_{\text{solid}} \qquad \Delta G = 40\frac{\text{kJ}}{\text{mole}} \quad (22)$$

$$H_2S + e \xrightarrow{\text{electric arc}} \dot{S}H + \dot{H} - 4\text{eV} \qquad \Delta G = -401\frac{\text{kJ}}{\text{mole}} \quad (23)$$

$$H\dot{S} + H\dot{S} \rightarrow S + H_2S + 0.39\ \text{eV} \qquad \Delta G = 53\frac{\text{kJ}}{\text{mole}} \quad (24)$$

$$S + H_2S \rightarrow H_2 + S_2 + 1.83\ \text{eV} \qquad \Delta G = 171\frac{\text{kJ}}{\text{mole}} \quad (25)$$

$$2S \rightarrow S_2 \qquad \Delta G = -144\frac{\text{kJ}}{\text{mole}} \quad (26)$$

$$4S_2^{gas} \rightarrow S_8 \qquad \Delta G = -20\frac{\text{kJ}}{\text{mole}} \quad (27)$$

$$H + H \rightarrow H_2 \qquad \Delta G = -427\frac{\text{kJ}}{\text{mole}} \quad (28)$$

Reaction (23) is endothermic, whereas (24) and (25) are exothermic. To compensate for the energy expenditure on the endothermic reaction (23), the process can be carried out with small additions of oxygen, during which radical formation reactions and by-product reactions will occur [66].

Under the influence of electrons generated by the arc discharge, molecular oxygen breaks down into atomic oxygen, which may subsequently result in the formation of alkyl peroxide compounds [67,68]:

$$O_2 + e \rightarrow 2\dot{O} \quad (29)$$

$$\dot{C}H_3 + O_2 \rightarrow CH_3O\dot{O} \quad (30)$$

Further transformations of alkylperoxy radicals influence the branching pathways in the conversion of hydrogen sulfide within the steam–gas mixture containing methane. Methylperoxy radicals primarily undergo disproportionation, resulting in the formation of methoxy radicals and molecular oxygen. These products then participate in the decomposition of hydrogen sulfide, leading to the generation of methanol and the $HS^{\bullet}$ radical. Additionally, alkyl radicals contribute to the decomposition of hydrogen sulfide [69].

$$CH_3\dot{O} + H_2S \rightarrow CH_3OH + H\dot{S} \quad (31)$$

$$\dot{C}H_3 + H_2S \rightarrow CH_4 + H\dot{S} \quad (32)$$

The route for the incomplete oxidation of hydrogen sulfide, described by a reaction similar to the Claus process [70], is also possible.

$$H_2S + O_2 \rightarrow S_2 + 2H_2O \quad (33)$$

$$H_2S + xO_2 \rightarrow (1 - 2x)H_2 + 2xH_2O + S_{solid}, \quad \Delta H^0_{298} = 0.21 - 5.01x, eV \quad (34)$$

Data obtained from gas chromatography of condensed phases indicate the production of only two oxygenated carbon derivatives: methanol and ethanol (Table 9).

Table 9. Data from gas chromatography of condensed phases of cavitation-jet water treatment under the influence of an electric arc (sample from the cooler).

Ret Time	Name of Product	Cold Container (T = 23 °C)
		Amount [mg/mL]
2.522	Methanol	3.17×10^{-4}
2.642	Ethanol	1.17×10^{-4}

Thus, the distinctive aspect of the decomposition reaction of hydrogen sulfide, rather than that of water, carbon dioxide, or methane, is the enhancement it experiences due to its organization under low-temperature plasma conditions. This enhancement is achieved through the integration of hydrodynamic cavitation and electric arc discharge.

Figure 7 illustrates the XRD analysis data for deposits on the surfaces of the Venturi tube's swirlers (a) and the suspension (b) filtered in residual water, which underwent cavitation-jet treatment influenced by an electric arc with the introduction of gaseous hydrogen sulfide. The deposit on the surface of the vortex tube consists of a mixture of barium hydroxide ($Al(OH)_3$ PDF 74-1119, 86.5 wt.%) and sulfur (αS_8 PDF 78-1889, 13.5 wt.%). The white deposit on the reflector's surface is exclusively composed of bayerite, a subject previously addressed in our work [25].

A specific focus is the deposit (Figure 8), which includes the sulfur modification SI (αS8, PDF 78-1889, 46.6 mass%) and an additional form, SII (S_8, PDF 71-0396, 17.0 mass%). This deposit also contains barite and two sulfur modifications, as well as reflections indicative of magnetite (Fe_3O_4, PDF 89-0951, 26.9 mass%) and iron sulfide ($Fe_{0.9}S$, PDF 75-2377, 1.5 mass%). The formation of magnetite and iron sulfide occurs during cavitation-jet gas-liquid flow, which is influenced by an electric discharge in the presence of hydrogen sulfide. Structural elements of the CJR play a role, particularly the attachment of the reflector in the reactor, which is made from an iron plate positioned behind the Laval nozzle. During the decomposition of hydrogen sulfide molecules into hydrogen and gaseous sulfur within the cavitation nuclei formation zone, and under the influence of an electric discharge, sulfur atoms are likely to dimerize. This process results in the formation of colloidal particles with a globular structure. Diatomic gaseous sulfur shows significant solubility in water, leading to nucleation characterized by the creation of a condensed hydrophilic phase within an aqueous dispersion medium [71].

The morphology of the isolated deposits was analyzed using scanning electron microscopy, as shown in Figure 8. The deposits formed in the volume of the solution (dark gray precipitate) differ significantly from those on the surface of structural elements, such as the swirl and the flow reflector of the gas–liquid mixture (light-colored precipitate). The deposits filtered from the liquid after stopping the CJR primarily consist of porous formations made up of globular particles, which are agglomerates of molecular sulfur in two distinct modifications. The white deposits exhibit porous and layered structures, mainly composed of magnetite, along with aluminum and iron sulfides. The spaces in

these structures are filled with micro-particles, predominantly in a globular shape, likely consisting of sulfur.

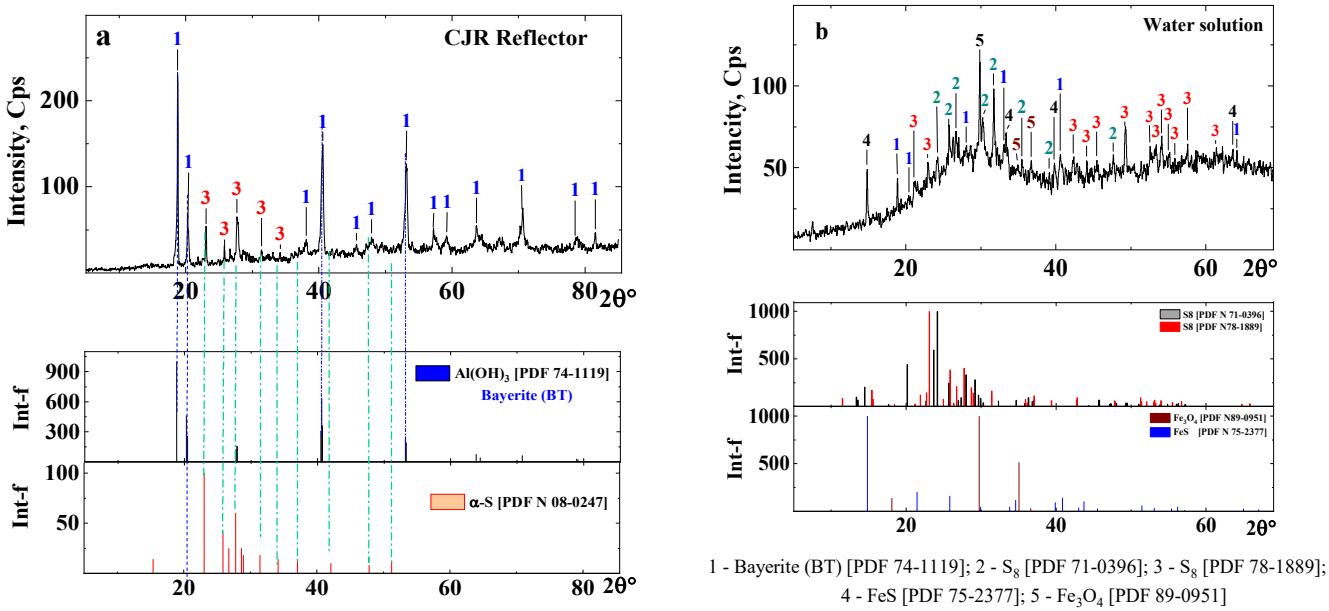

1 - Bayerite (BT) [PDF 74-1119]; 2 - S_8 [PDF 71-0396]; 3 - S_8 [PDF 78-1889]; 4 - FeS [PDF 75-2377]; 5 - Fe_3O_4 [PDF 89-0951]

Figure 7. XRD data for deposits on the surface of a CJR reflector (**a**) and in water solution (**b**) formed during cavitation-jet treatment under the influence of an electric arc discharge of distilled water containing hydrogen sulfide molecules.

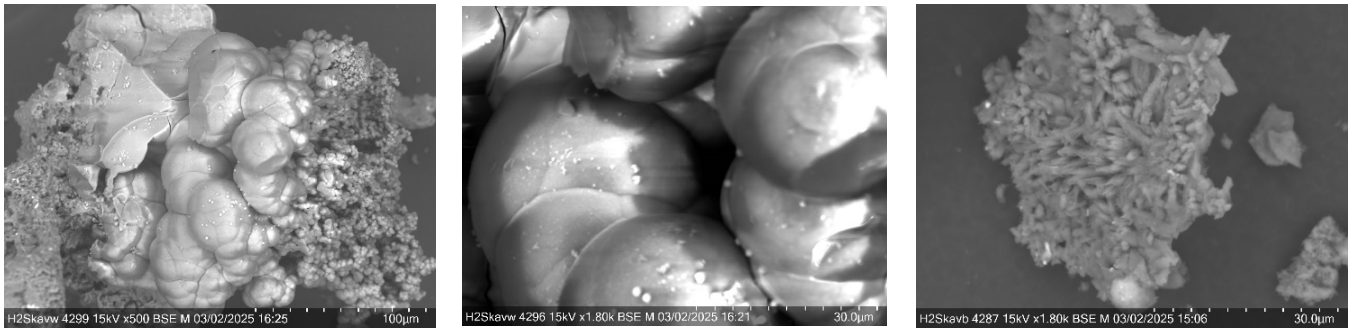

(**a**) Solution deposit H_2S–H_2O.

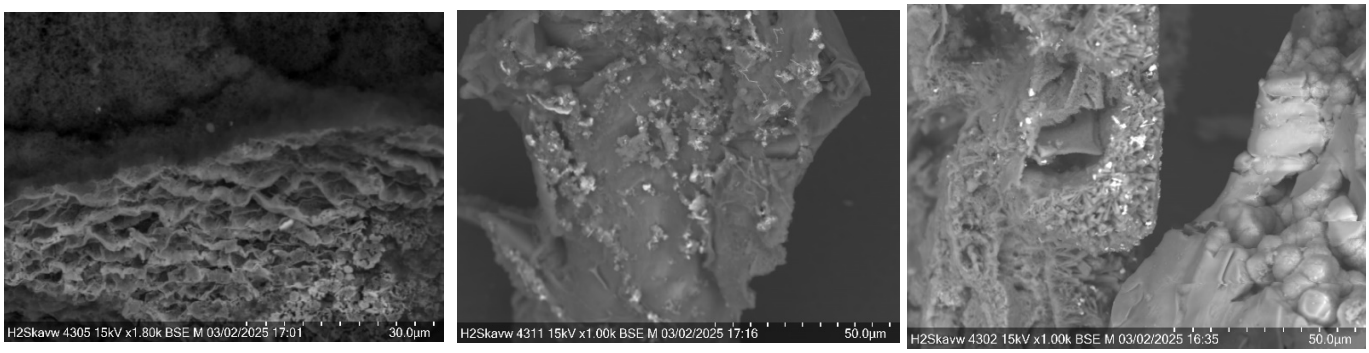

(**b**) Reflector deposit H_2S–H_2O.

Figure 8. SEM data of deposits formed in the solution and on the surface of the CJR reflector.

SEM images demonstrate clusters of irregularly shaped particles with a rough surface and pronounced microtexture, characteristic of aggregates with heterogeneous phase structures. The surface of the deposits obtained in water at maximum magnification shows that they consist of rounded, granular formations—predominantly spherical or

hemispherical particles of various sizes (Figure 8, first row). Some of them have light spots or deposits, which may indicate the presence of secondary phases or sediments and the heterogeneity of the composition or distribution of components.

The surface of the deposits formed on the reflector and the swirler of the cavitating jet flow of the steam–gas mixture (Figure 8, bottom row) demonstrates a pronounced layered and porous texture. Fibrous or fragmented areas are observed, which may indicate the microporosity of the material. The particles are aggregated, have irregular shapes, and vary in size, which may indicate a micro- or nanostructured surface.

On the surface of metal sulfides, conditions are established that allow for a chemical reaction that is thermodynamically prohibited in the gas phase [71,72]. This renders the process irreversible. Consequently, the surface reaction leads to the separation of the products from the hydrogen sulfide dissociation reaction, accompanied by the release of molecular hydrogen, as illustrated by the following equation and scheme:

$$2(H_2S) \xrightarrow{Me_xS_{y(katalyst)}} (H_2S_2)_{abs} + H_2 \qquad \Delta G = 30\ kJ/mole \tag{35}$$

$$(H_2S_2)_{abs} \rightarrow H_2 + 1/8S_8 \qquad \Delta G = -140\ kJ/mole \tag{36}$$

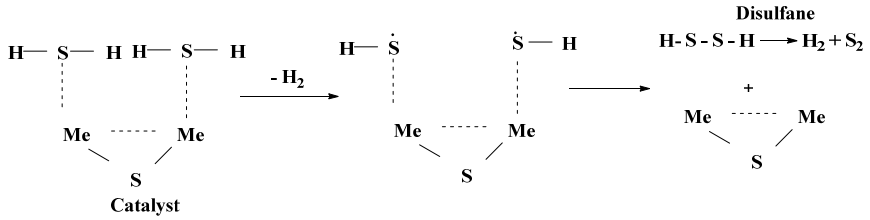

(37)

The formation of two modifications of S8 is also detected in the XRD analysis data (Figure 7). The process of hydrogen sulfide decomposition on the surface of metal sulfides (catalysts) is exothermic and occurs with a decrease in Gibbs energy, resulting in the formation of molecular hydrogen and solid modifications of singlet sulfur (S_8^{I} and S_8^{II}, respectively).

The formation of disulfane can be visually detected in the residual water due to its yellowish, oily color and distinct odor. While disulfane is considered a stable compound, it can gradually decompose in the presence of air, resulting in the formation of hydrogen sulfide and elemental sulfur. This decomposition is evident when drying an aqueous suspension that has a yellowish tint, particularly after undergoing cavitation-jet treatment in an arc discharge.

3.2.3. System H_2O–H_2S–CH_4

Table 10 presents the relative contents of gas mixtures recorded by the gas sensor at various times during the cavitation-jet treatment of distilled water containing CH_4 (methane) and H_2S (hydrogen sulfide) under the influence of an electric arc discharge. It is observed that when hydrogen sulfide and methane are introduced into the circulating liquid at the 15th minute of the cavitation-jet reactor's operation, and the temperature of the vapor–gas mixture reaches 40 °C, there is a decrease in the concentrations of CO (carbon monoxide) and O_2 (oxygen), along with a noticeable increase in molecular hydrogen content (from 18 mg/m^3 to 32 mg/m^3). The expected decrease in the proportion of hydrogen sulfide and methane molecules occurs as they undergo dissociation due to the conditions of steam–gas cavitation and the influence of an electric arc discharge on the GVL flow in the cavitation-jet reactor, as noted in Sections 3.2.1 and 3.2.2. In contrast to methane, the reduction in hydrogen sulfide concentration is significant, decreasing from 100 mg/m^3 to 84 mg/m^3 and from 152 mg/m^3 to 17 mg/m^3, respectively.

Table 10. Relative contents of gas mixtures recorded by the gas sensor at different treatment times (H_2O–H_2S–CH_4) [1].

Gas Composition	Unit/Notes	CJT		EAD	
		Total Processing Time, min			
		10	15	20	50
t, °C	°C	30°	40°	60°	83°
H_2	mg/m^3	16	18	32	29
CO	mg/m^3	80	474	131	36
CH_4	%LEL	0	100 [1,2]	97	84
H_2S	mg/m^3	0	152 [1,3]	48	17
O_2	vol.%	19.4	13.4	11.5	21.8

[1] The detection limit of the gas sensor; [2] supply of methane from the gas cylinder; [3] supply of hydrogen sulfide from the gas cylinder.

The gas chromatographic–mass spectrometric analysis data (Table 11) reveal a trend of decreasing concentrations of methane, nitrogen, and oxygen in the vapor–gas mixture before (OC No. 1, CJT) and after (OC No. 2 and No. 3, EAD) exposure to an electric arc discharge in the cavitating-jet flow. An increase in the concentration of gaseous H_2 is noted, and the absence of free hydrogen sulfide supports the conclusion regarding its recorded residual content in the gas–vapor phase.

Table 11. Relative proportions of gas mixtures recorded at different inlets in the mass spectrometer chamber (H_2O–H_2S–CH_4) [1].

Mass Number (M)	Probable Substances	Inlet Source into the Mass Spectrometer Chamber		
		CJT, 50 °C	EAD, 60 °C (Moment of Supply of the Mixture of H_2S and CH_4)	EAD, 83 °C (After Treatment with a Mixture of H_2S and CH_4)
		OC №1, %	OC №2, %	OC №3, %
2	H_2	0.18	0.27	0.32
12	C	0.01	0.17	0.01
16	CH_4	1.26	12.39	1.00
18	H_2O	1.04	0.96	0.79
28	N_2	80.40	79.06	68.56
32	O_2	15.99	16.5	14.40
40	Ar	1.09	1.10	1.08
44	CO_2	0.03	0.05	0.06

[1] The composition of the gas was determined in the oxygen cushion (OC) after the nitrogen trap at the outlet of the CJR.

The absence of residual hydrogen sulfide can be attributed to the presence of hydrocarbons, which promotes the maximum dissociation of hydrogen sulfide into either elemental sulfur or metal sulfides. These products comprise the primary working elements of the cavitation-jet reactor. It is important to note that when the CH_4–H_2S mixture is introduced into the gas–vapor phase of the reactor during an electric arc discharge, there is a significant increase in carbon atoms, rising from 0.01 mass % to 0.17 mass %. This increase is followed by a decrease as the temperature reaches 83 °C.

The formation of new products (acetone, methanol, ethanol, and acetonitrile) during the low-temperature plasma-chemical process is also confirmed by the data from liquid chromatography of condensed phases (Table 12). It is evident that all the reaction products belong to the category of volatile organic compounds, which easily condense and are captured in the first cooling circuit by the water cooler.

Table 12. Data on liquid chromatography of condensed phases from cavitation-jet water treatment under the influence of an EAD.

Ret Time	Name of Product	Hot Container T = 80 °C	Water Cooler T = 11 °C
		Amount [mg/mL]	
2.414	Acetone	4.72×10^{-5}	5.12×10^{-4}
2.522	Methanol	1.62×10^{-4}	1.37×10^{-3}
2.642	Ethanol	1.42×10^{-4}	3.44×10^{-4}
2.794	Acetonitrile	5.23×10^{-5}	8.4×10^{-4}

The absence of hydrogen sulfide may indicate that the dissociation process in the presence of methane occurs at a high speed, almost instantaneously, resulting in the formation of metal sulfides. The obtained data are in good agreement with the findings of works [71,72], which detailed the plasma-chemical processes of hydrogen sulfide conversion in barrier and arc discharge in the presence of CO_2 and gaseous and liquid hydrocarbons. In all the cited works, the conversion rate of hydrogen sulfide reached nearly 100%. The only difference between the cited works and our experiments is that they were conducted at atmospheric or elevated pressure.

The complete loss of hydrogen atoms in the methane molecule is confirmed by TDS analysis data and XRD deposits formed on the internal parts of the CJR, in the residual water, and in the oxygen cushion after the nitrogen trap, respectively.

The SEM image data (Figure 9) reveal active microstructural transformations typical of plasma-chemical treatment. The observed granules, layered structures, and porosity suggest a multi-phase system, which is further supported by the XRD results (Figure 10). These results indicate the formation of mixed aluminum and iron carbides, their sulfides, and aluminum oxide derivatives. The surface exhibits a dense aggregation of particles characterized by a pronounced rough texture, with the particles being irregularly shaped and varying in size.

The data from XRD, TDS, and SEM analyses indicate that cavitation-jet treatment of water, in the presence of hydrogen sulfide and its mixture with methane, leads to the formation of iron and aluminum sulfides (Figures 8 and 10). These compounds may serve as sulfide catalysts for the decomposition of H_2S into sulfur and hydrogen, facilitated by the intermediate formation of disulfane (Equation (37)). The formation of aluminum sulfides begins on the surfaces of aluminum structural components, such as the liquid swirler in the Venturi tube and the vapor–gas–liquid flow reflector located after the Laval nozzle exit.

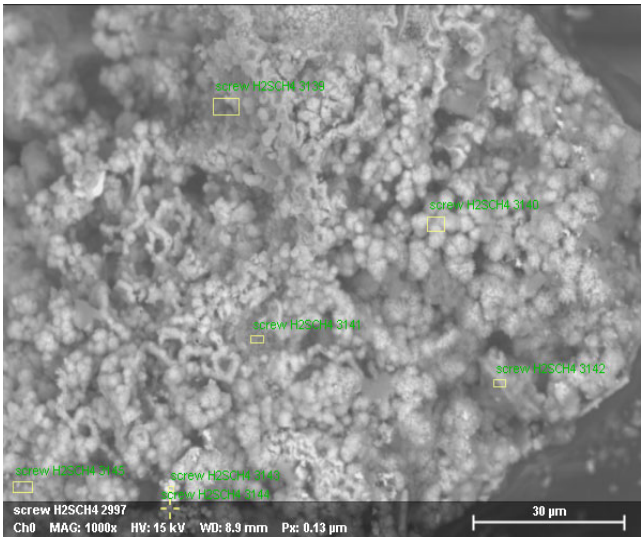

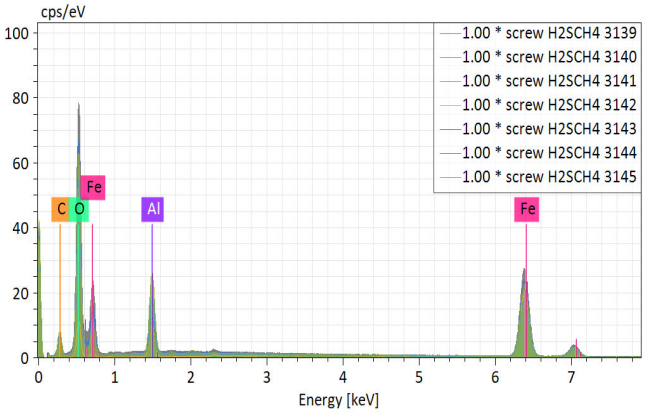

Spectrum	C	O	Al	Fe
screw H2SCH4 3139	12.56	39.48	6.96	41.00
screw H2SCH4 3140	11.74	23.20	5.42	59.65
screw H2SCH4 3141	11.23	32.13	4.64	51.99
screw H2SCH4 3142	15.73	13.56	6.80	63.91
screw H2SCH4 3143	9.90	38.52	4.07	47.51
screw H2SCH4 3144	8.69	39.09	3.07	49.14
screw H2SCH4 3145	12.09	38.37	8.47	41.07

Screw Deposit (A)

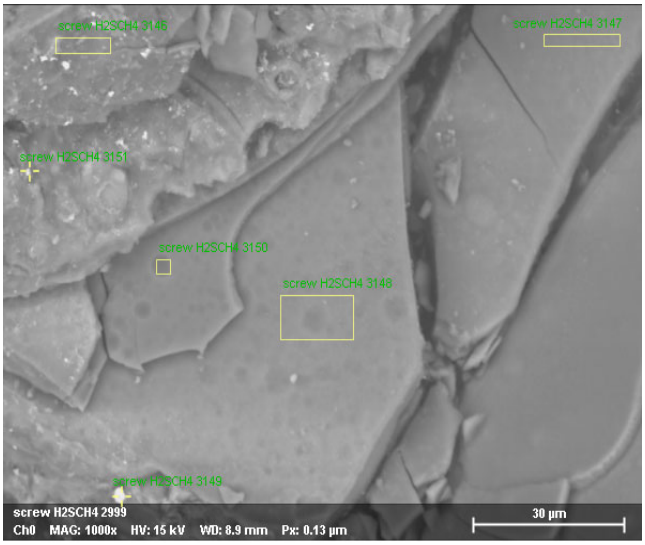

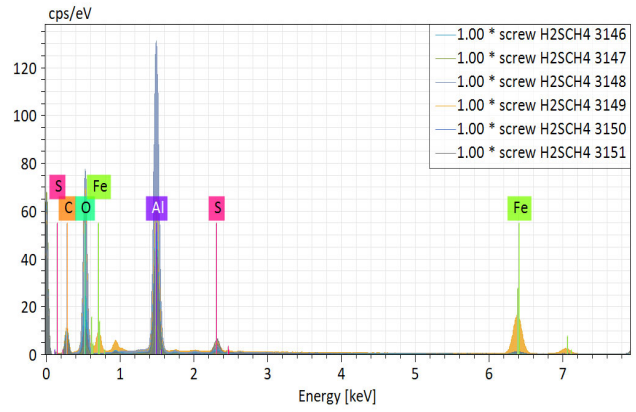

Spectrum	C	O	Al	S	Fe
screw H2SCH4 3146	31.08	41.83	22.88	1.03	3.18
screw H2SCH4 3147	51.84	28.93	17.80		1.43
screw H2SCH4 3148	14.63	53.34	31.19	0.83	
screw H2SCH4 3149	15.99	39.59	16.15	1.09	27.17
screw H2SCH4 3150	34.71	37.03	25.28	1.14	1.84
screw H2SCH4 3151	37.56	29.20	24.71	4.15	4.38

Reflector Deposit (B)

Figure 9. SEM data of deposits formed on the surface of different parts of the CJR screw after cavitation-jet treatment of water in an electric arc with the addition of a mixture of H_2S–CH_4.

Consequently, the thermodynamically permissible process of hydrogen sulfide decomposition on sulfide catalysts at room temperature into hydrogen and solid sulfur is achieved through the adsorption of disulfane, a critical surface intermediate [71]. Nevertheless, the initiation of this process in the gas phase is impossible without the involvement of a surface catalyst, which can be acquired by cavitating solid metal elements in a cavitation-jet reactor.

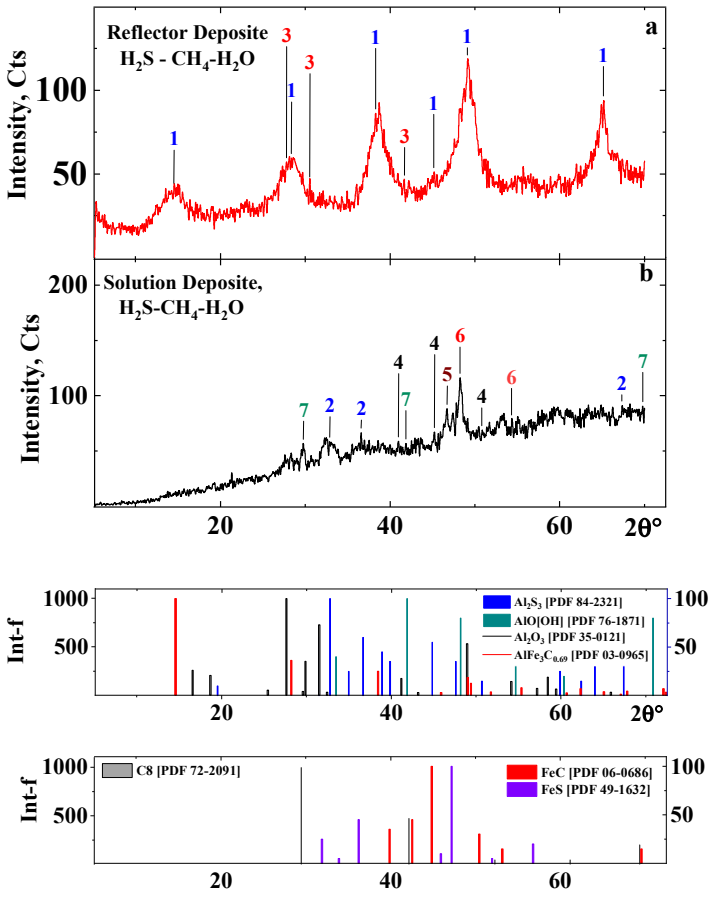

Figure 10. XRD analysis data of deposits formed on the CJR reflector: (**a**) and in solution (**b**) after cavitation-jet treatment of water with the addition of H_2S and CH_4 under the influence of an electric arc discharge.

4. Conclusions

This study investigates the feasibility of employing and processing sour-related petroleum gases via a cavitation-jet reactor integrated with an electric arc discharge (EAD). This combination amplifies the ionization of neutral molecules, resulting in the generation of chemically reactive ion-radical or radical species. The ensuing recombination of these particles yields hydrogen molecules, crystalline sulfur, and oxygen-containing organic carbon compounds.

The mechanisms and pathways of plasma-chemical processes under low-temperature plasma conditions have been experimentally validated based on previously proposed theories. The processes result from a synergistic effect of cavitating-jet flow and arc discharge, causing the molecular destruction of neutral gaseous molecules, including hydrogen sulfide, carbon dioxide, and water vapor. During the cavitating-jet flow of a vapor–gas–liquid mixture, weakly ionized plasma is generated, leading to the formation of intermediate active particles such as hydroxyl radicals ($OH^{\bullet}$), hydroperoxyl radicals ($HOO^{\bullet}$), atomic hydrogen ($H^{\bullet}$), and atomic oxygen ($O^{\bullet}$). The emission of weakly ionized plasma facilitates the formation of hydrogen peroxide (H_2O_2) and superoxide anions (O_2^-), which in turn promote the dissociation of water molecules.

The analysis of X-ray diffraction (XRD), thermodesorption spectroscopy (TDS), and scanning electron microscopy (SEM) data indicates that the cavitation-jet treatment of

water, in the presence of hydrogen sulfide and its mixture with methane, results in the formation of iron and aluminum sulfides, which constitute certain structural elements of the reactor. Metal sulfides act as catalysts in the decomposition of H_2S into sulfur and hydrogen, resulting in the formation of an intermediate disulfide.

The surface of metal sulfides facilitates chemical reactions that are thermodynamically prohibited in the gas phase, rendering the decomposition of hydrogen sulfide irreversible. This process leads to the dissociation of the acid gas, resulting in the formation of sulfur and molecular hydrogen.

The combination of cavitating-jet flow and electric arc discharge creates a truncated low-temperature plasma zone, which facilitates the production of hydrogen, two forms of S_8 (S_8^{I} and S_8^{II}), crystalline carbon, and various oxygen-containing compounds, including methanol, ethanol, acetone, and acetonitrile.

The proposed work facilitates the prediction of outcomes in the processing of associated petroleum gas by establishing a zone of non-equilibrium plasma formation within a cavitation-jet chamber in combination with an electric arc discharge, which can produce a substantial quantity of ionized active particles and radicals.

Author Contributions: Conceptualization, G.M.; funding acquisition, G.M.; investigation, G.M., I.D. and Y.N.; methodology, G.M., A.B. and V.T.; project administration, G.M.; resources, I.D., Y.N., A.B. and V.T.; supervision, G.M.; validation, G.M. and I.D.; visualization, G.M. and I.D.; writing—original draft, G.M.; writing—review and editing, G.M. and I.D. All authors have read and agreed to the published version of the manuscript.

Funding: This research was funded by Institute of Nuclear Physics, Almaty, grant number 136434/Initiative-OT-25, titled "Development of a technology for a radiation-chemical method for the utilization of associated petroleum and greenhouse gases (APG and GHG) to produce hydrogen and associated products with high added value".

Data Availability Statement: The original contributions presented in this study are included in the article; further inquiries can be directed to the corresponding author.

Acknowledgments: During the preparation of this manuscript, the author(s) used an AI tool (ChatGPT-5.1) for the purposes of creation of Graphical abstract. The relevant information is included on the graphic abstract image. The authors have reviewed and edited the output and take full responsibility for the content of this publication.

Conflicts of Interest: The authors declare no conflicts of interest.

Abbreviations

The following abbreviations are used in this manuscript:

APG	associated petroleum gas
CAP	chemically active plasma
CJC	cavitation-jet chamber
CJR	cavitation-jet reactor
CJT	cavitation-jet treatment
EAD	electric arc discharge
EDS	energy dispersive analysis
GVL	gas–vapor–liquid
LEL	Lower Explosive Limit
LGM	liquid–gas mixture
LN	Laval nozzle
LTP	low-temperature plasma technology
NEP	non-equilibrium plasma
OC	oxygen cushion

SCW	supercritical water
SEM	Scanning electron microscopy
TDS	Thermal Desorption Spectrometry
VT	Venturi tube
XRD	X-ray diffraction analysis

References

1. Garipov, A.; Khomenko, A. Comparison of economic and material costs for the purification of associated petroleum gas from hydrogen sulfide and carbon dioxide. *Vestn. Kazan Technol. Univ.* **2016**, *19*, 53–55. (In Russian)
2. Bulaev, S.A. Flaring of associated petroleum gases: Analysis of past years and state regulation. *Vestn. Kazan Technol. Univ.* **2013**, *16*, 202–205. (In Russian)
3. Fan, T.; Li, M.; Liu, Z.; Zhao, Y.; Ma, Y. Study on associated gas combustion characteristics and inert gas influence rules in air-foam flooding process. *Fuel* **2021**, *302*, 121140. [CrossRef]
4. Popov, N.V.; Govor, I.L.; Gitarskii, M.L. Greenhouse gas emission from combustion of associated petroleum gas in Russia. *Russ. Meteorol. Hydrol.* **2021**, *46*, 325–330. [CrossRef]
5. International Energy Agency. *Net Zero by 2050: A Roadmap for the Global Energy Sector*; IEA: Paris, France, 2021.
6. Mazzucato, M. Mission-oriented innovation policies: Challenges and opportunities. *Ind. Corp. Change* **2018**, *27*, 803–815. [CrossRef]
7. Barjasteh, A.; Dehghani, Z.; Lamichhane, P.; Kaushik, N.; Choi, E.H.; Kaushik, N.K. Recent Progress in Applications of Non-Thermal Plasma for Water Purification, Bio-Sterilization, and Decontamination. *Appl. Sci.* **2021**, *11*, 3372. [CrossRef]
8. Nguyen, V.T.; Nguyen, D.B.; Heo, I.; Mok, Y.S. Plasma-Assisted Selective Catalytic Reduction for Low-Temperature Removal of NOx and Soot Simulant. *Catalysts* **2019**, *9*, 853. [CrossRef]
9. Clerici, M.; Hu, Y.; Lassonde, P.; Milian, C.; Couairon, A.; Christodoulides, D.N.; Chen, Z.; Razzari, L.; Vidal, F.; Legare, F.; et al. Laser-assisted guiding of electric discharges around objects. *Sci. Adv.* **2015**, *1*, e1400111. [CrossRef] [PubMed]
10. Longe, P.; Effiong, A.; Danso, D.K. Predicting hydrogen solubility in water with gradient boosting and LightGBM. *Acad. Green Energy* **2025**, *2*, 1–18. [CrossRef]
11. Luo, Y.; Wu, Z.; Li, Z.; Cheng, L.; Qi, P.; Mou, J. Design of a Novel Pump Cavitation Valve and Study of Its Cavitation Characteristics. *Water* **2025**, *17*, 1503. [CrossRef]
12. Lyu, F.; Tang, M.; Zhou, F.; Zhang, X.; Han, S.; Zhang, S. Research on the Effect of Structural Parameters on Cavitation Performance of Shear Hydrodynamic Cavitation Generator. *Appl. Sci.* **2024**, *14*, 3676. [CrossRef]
13. Luo, C.; Gu, J. Surface Properties and Cavitation Erosion Resistance of Cast Iron Subjected to Laser Cavitation Treatment. *Metals* **2023**, *13*, 1793. [CrossRef]
14. Amin, A. Review of autothermal reactors: Catalysis, reactor design, and processes. *Int. J. Hydrogen Energy* **2024**, *65*, 271–291. [CrossRef]
15. Nitsche, T.; Unger, C.; Weidner, E. Plasma catalytic reactors for atmospheric gas conversions. *Chem. Ing. Tech.* **2018**, *90*, 1453–1464. [CrossRef]
16. Ulejczyk, B.; Nogal, Ł.; Jóźwik, P.; Młotek, M.; Krawczyk, K. Plasma-catalytic process of hydrogen production from mixture of methanol and water. *Catalysts* **2021**, *11*, 864. [CrossRef]
17. Fan, D.; Gao, Y.; Liu, F.; Wei, T.; Ye, Z.; Ling, Y.; Chen, B.; Zhang, Y.; Ni, M.; Dong, D. Autothermal reforming of methane over an integrated solid oxide fuel cell reactor for power and syngas co-generation. *J. Power Sources* **2021**, *513*, 230536. [CrossRef]
18. Ampaya, J.P.; Rinker, R.G. Autothermal reactors with internal heat exchange: Numerical and experimental studies. *Chem. Eng. Sci.* **1977**, *32*, 1327–1338. [CrossRef]
19. Batrakov, P.A.; Ryzhnikova, E.A.; Batrakova, A.A. The Use of Associated Petroleum Gas by Burning it in a Mixture with Natural Gas in a Combined Cycle Gas Plant to Generate Mechanical Energy and Electricity. In *Proceedings of the 2024 Dynamics of Systems, Mechanisms and Machines (Dynamics), Omsk, Russia, 12–14 November 2024*; IEEE: Piscataway, NJ, USA, 2024; pp. 1–8. [CrossRef]
20. Rusanov, V.D.; Fridman, A.A.; Sholin, G.V. Physics of chemically active plasma with nonequilibrium vibrational excitation of molecules. *Usp. Fiz. N.* **1981**, *134*, 185–235. (In Russian) [CrossRef]
21. Ghimire, B.; Lamichhane, P.; Lim, J.S.; Min, B.; Paneru, R.; Weltmann, K.-D.; Choi, E.H. An atmospheric pressure plasma jet operated by injecting natural air. *Appl. Phys. Lett.* **2018**, *113*, 194101. [CrossRef]
22. Geng, L.; Chen, J.; De La Torre, O.; Escaler, X. Numerical Simulation of Cavitation Erosion Aggressiveness Induced by Unsteady Cloud Cavitation. *Appl. Sci.* **2020**, *10*, 5184. [CrossRef]
23. Toth, J.R.; Abuyazid, N.H.; Lacks, D.J.; Renner, J.N.; Sankaran, R.M. Plasma-water droplet reactor for continuous nitrogen fixation. *ACS Sustain. Chem. Eng.* **2020**, *8*, 14845–14854. Correction in *ACS Sustain. Chem. Eng.* **2020**, *9*, 599–600. https://doi.org/10.1021/acssuschemeng.0c08763. [CrossRef]

24. Mamytbekov, G.; Shayakhmetov, N.; Aizhulov, D.; Kurmanseiit, M.; Tungatarova, M. Transport of Steam-Gas Mixture in Hydrodynamic Devices: A Numerical Study of Steam Reforming of Methane. *Processes* **2023**, *11*, 2991. [CrossRef]
25. Mamytbekov, G.K.; Danko, I.V.; Beksultanov, Z.I.; Nurtazin, Y.R.; Rakhimbayev, A. Perspectives of Hydrogen Generation in Cavitation–Jet Hydrodynamic Reactor. *Appl. Sci.* **2024**, *14*, 9415. [CrossRef]
26. Danko, I.; Bekbaev, A.; Mamytbekov, G.; Sarsenbayev, E.; Minazhova, S. Information and measurement system of a hydrodynamic cavitation-jet reactor for hydrogen generation. *Vestn. KazATK* **2025**, *138*, 488–499. (In Russian)
27. Miklos, D.B.; Remy, C.; Jekel, M.; Linden, K.G.; Drewes, J.E.; Hübner, U. Evaluation of advanced oxidation processes for water and wastewater treatment. *Water Res.* **2018**, *139*, 118–131. [CrossRef]
28. Shakir, S.W.; Ahmed, S.M.R.; Wiheeb, A.D. Improvement of CO_2 absorption/desorption rate using new nanofluid. *Int. J. Heat Technol.* **2021**, *39*, 851–857. [CrossRef]
29. Bogaerts, A.; Neyts, E.C. Plasma technology: An emerging technology for energy storage. *ACS Energy Lett.* **2018**, *3*, 1013–1027. [CrossRef]
30. Shivkumar, G.; Tholeti, S.S.; Alrefae, M.A.; Fisher, T.S.; Alexeenko, A.A. Analysis of hydrogen plasma in a microwave plasma chemical vapor deposition reactor. *J. Appl. Phys.* **2016**, *119*, 113301. [CrossRef]
31. Kuzmin, G.P.; Minaev, I.M.; Rukhadze, A.A.; Tikhonevich, O.V. Temperature dependence of the characteristics of electrical discharge in water vapor. *Kratk. Soobshch. Fiz. FIAN* **2010**, *7*, 38–42. (In Russian)
32. Panda, D.; Saharan, V.K.; Manickam, S. Controlled Hydrodynamic Cavitation: A Review of Recent Advances and Perspectives for Greener Processing. *Processes* **2020**, *8*, 220. [CrossRef]
33. Lv, L.V.; Luo, X.; Zhang, H.; Cui, B.; Chen, L. Numerical investigation on bubble interaction dynamics in hydrodynamic cavitation. *Mechanika* **2021**, *27*, 115–121. [CrossRef]
34. Bandala, E.R.; Rodriguez-Narvaez, O.M. On the Nature of Hydrodynamic Cavitation Process and Its Application for the Removal of Water Pollutants. *Air Soil Water Res.* **2019**, *12*, 1178622119880488. [CrossRef]
35. Suslick, K.S.; Mdleleni, M.M.; Ries, J.T. Chemistry induced by hydrodynamic cavitation. *J. Am. Chem. Soc.* **1997**, *119*, 9303–9304. [CrossRef]
36. Yasui, K.; Towata, A.; Tuziuti, T.; Kozuka, T.; Kato, K. Effect of static pressure on acoustic energy radiated by cavitation bubbles in viscous liquids under ultrasound. *J. Acoust. Soc. Am.* **2011**, *130*, 3233–3242. [CrossRef] [PubMed]
37. Fleite, S.N.; Ayude, M.A.; Ranade, V.V.; Cassanello, M.C. Hydrodynamic cavitation effects on advanced oxidation processes and mass transfer: A conceptual model. *Chem. Eng. J. Adv.* **2024**, *18*, 100603. [CrossRef]
38. Nikitenko, S.I. Plasma formation during acoustic cavitation: Toward a new paradigm for sonochemistry. *Adv. Phys. Chem.* **2014**, *2014*, 173878. [CrossRef]
39. Goncharuk, V.V.; Malyarenko, V.V.; Yaremenko, V.A. Use of ultrasound in water treatment. *J. Water Chem. Technol.* **2008**, *30*, 137–150. [CrossRef]
40. Efremova, K.D.; Pil'gunov, V.N. Cavitation properties of liquids. *Sci. Educ. Bauman MSTU. Electron. J.* **2016**, *3*, 12–36. (In Russian) [CrossRef]
41. Shao, W.-H.; Chen, W.-Z. Effect of supercritical water shell on cavitation bubble dynamics. *Chin. Phys. B* **2015**, *24*, 054701. [CrossRef]
42. Galkin, A.A.; Lunin, V.V. Subcritical and supercritical water: A universal medium for chemical reactions. *Russ. Chem. Rev.* **2005**, *74*, 21–35. [CrossRef]
43. Maxim, F.; Contescu, C.; Boillat, P.; Niceno, B.; Karalis, K.; Testino, A.; Ludwig, C. Visualization of supercritical water pseudo-boiling at Widom line crossover. *Nat. Commun.* **2019**, *10*, 4114. [CrossRef]
44. Tsubaki, N.; Ito, M.; Fujimoto, K. A new method of low-temperature methanol synthesis. *J. Catal.* **2001**, *197*, 224–227. [CrossRef]
45. Sheppard, T.; Hamill, C.D.; Goguet, A.; Rooney, D.W.; Thompson, J.M. A low-temperature isothermal gas-phase system for conversion of methane to methanol over Cu–ZSM-5. *Chem. Commun.* **2014**, *50*, 11053–11055. [CrossRef] [PubMed]
46. Qi, C.; Bi, Y.; Yu, H.; Zhang, H.; Zhang, Q.; Wang, X.; Fan, M.; Wang, M.; Wu, M.; Wu, W. One-Step Synthesis of Methanol from CH_4 and CO_2 by a Plasma Synergistic Catalyst. *Ind. Eng. Chem. Res.* **2024**, *63*, 9576–9583. [CrossRef]
47. Lebarbier, V.M.; Dagle, R.A.; Kovarik, L.; Lizarazo-Adarme, J.A.; King, D.L.; Palo, D.R. Synthesis of methanol and dimethyl ether from syngas over $Pd/ZnO/Al_2O_3$ catalysts. *Catal. Sci. Technol.* **2012**, *2*, 2116. [CrossRef]
48. Sophiana, I.C.; Adhi, T.P.; Budhi, Y.W. Simulation of Dry Reforming of Methane to Form Synthesis Gas as Feed Stock for Acetic Acid Production. *MATEC Web Conf.* **2021**, *333*, 06002. [CrossRef]
49. Galanov, S.I.; Sidorova, O.I.; Gavrilenko, M.A. The process of acetonitrile synthesis over γ-Al_2O_3 promoted by phosphoric acid catalysts. *Procedia Chem.* **2014**, *10*, 108–113. [CrossRef]
50. Mamytbekov, G.; Shayakhmetov, N.; Aizhulov, D.; Kurmanseiit, M.; Tungatarova, M.; Zhakanbayev, Y.; Danko, I.; Rakhimbayev, A. Mathematical Modeling of the Transport of H_2O–CH_4 Steam–Gas Mixtures in Hydrodynamic Devices: The Role of Helical Screws. *Processes* **2024**, *12*, 2416. [CrossRef]

51. Iida, S.; Togo, H. Direct oxidative conversion of alcohols and amines to nitriles with molecular iodine and DIH in aqueous ammonia. *Tetrahedron* **2007**, *63*, 8274–8281. [CrossRef]
52. Oshanina, I.V.; Bruk, L.G.; Temkin, O.N. *Alternative Methods for Producing Products of Basic Organic Synthesis*; MITKhT: Moscow, Russia, 2002. (In Russian)
53. Machala, Z.; Tarabová, B.; Sersenová, D.; Janda, M.; Hensel, K. Chemical and Antibacterial Effects of Plasma Activated Water: Correlation with Gaseous and Aqueous Reactive Oxygen and Nitrogen Species, Plasma Sources and Air Flow Conditions. *J. Phys. D Appl. Phys.* **2018**, *52*, 034002. [CrossRef]
54. Hong, J.; Prawer, S.; Murphy, A.B. Production of ammonia by heterogeneous catalysis in a packed-bed dielectric-barrier discharge. *IEEE Trans. Plasma Sci.* **2014**, *42*, 2338–2339. [CrossRef]
55. Patil, B.S.; Wang, Q.; Hessel, V.; Lang, J. Plasma N_2-fixation: 1900–2014. *Catal. Today* **2015**, *256*, 49–66. [CrossRef]
56. Gutsol, K.; Robinson, R.; Rabinovich, A.; Gutsol, A.; Fridman, A. High conversion of hydrogen sulfide in gliding arc plasmatron. *Int. J. Hydrogen Energy* **2017**, *42*, 68–75. [CrossRef]
57. Mollah, M.Y.A.; Schennach, R.; Patscheider, J.; Promreuk, S.; Cocke, D.L. Plasma chemistry as a tool for green chemistry and waste management. *J. Hazard. Mater.* **2000**, *79*, 301–320. [CrossRef]
58. Wolf, M.; Gibson, E.K.; Olivier, E.J.; Neethling, J.H.; Catlow, C.R.A.; Fischer, N.; Claeys, M. In-depth characterisation of metal-support compounds in spent Co/SiO_2 catalysts. *Catal. Today* **2020**, *342*, 71–78. [CrossRef]
59. Tunå, P.; Hulteberg, C.; Ahlgren, S. Techno-economic assessment of nonfossil ammonia production. *Environ. Prog. Sustain. Energy* **2013**, *33*, 1290–1297. [CrossRef]
60. Taşdemir, A.; Cengiz, İ.; Yildiz, E.; Bayhan, Y.K. Investigation of ammonia stripping with a hydrodynamic cavitation reactor. *Ultrason. Sonochem.* **2020**, *60*, 104741. [CrossRef]
61. Zeghioud, H.; Nguyen-Tri, P.; Khezami, L.; Amrane, A.; Assadi, A.A. Review on discharge plasma for water treatment. *J. Water Process Eng.* **2020**, *38*, 101664. [CrossRef]
62. Janev, R.K.; Reiter, D. Collision processes of hydrocarbon species in hydrogen plasmas. Part 1. The methane family. *ChemInform* **2003**, *34*, 25. [CrossRef]
63. Kudryashov, S.V.; Ryabov, A.Y.; Ochered'ko, A.N. Oxidative plasma-chemical conversion of hydrogen sulfide. *Izv. Tomsk. Politekh. Univ.* **2016**, *327*, 76–85. (In Russian)
64. Vakar, A.K.; Zhivotov, V.K.; Zharskii, I.M.; Krasheninnikov, E.; Mikhail, N.I.; Rusanov, V.D.; Vladimir, Y.T. Study of hydrogen sulfide dissociation in a microwave discharge. *Vopr. At. Nauk. Tekh.* **1981**, *2*, 43–45. (In Russian)
65. Bagautdinov, A.Z.; Zhivotov, V.K.; Kalachev, I.A.; Krasheninnikov, E.G.; Novikov, G.I.; Rusanov, V.D.; Yavorsky, V.T. Study of radial distributions of gas flows. *Khim. Vys. Energ.* **1993**, *27*, 68–73. (In Russian)
66. Kudryashov, S.V.; Ryabov, A.Y.; Ochered'ko, A.N.; Krivtsova, K.B.; Shchyogoleva, G.S. Removal of hydrogen sulfide from methane in a barrier discharge. *Khim. Vys. Energ.* **2019**, *53*, 396–399. (In Russian) [CrossRef]
67. Benson, S.W. *Thermochemical Kinetics: Methods for the Estimation of Thermochemical Data and Rate Parameters*, 2nd ed.; Wiley: New York, NY, USA, 1976.
68. Atkinson, R.; Baulch, D.L.; Cox, R.A.; Crowley, J.N.; Hampson, R.F.; Hynes, R.G.; Jenkin, M.E.; Rossi, M.J.; Troe, J. Evaluated kinetic and photochemical data for atmospheric chemistry: Volume I—Gas phase reactions of O_x, HO_x, NO_x and SO_x species. *Atmos. Chem. Phys.* **2004**, *4*, 1461–1738. [CrossRef]
69. Mousavipour, S.H.; Pirhadi, F.; Habibagahi, A.A. Theoretical investigation on the kinetics of amidogen reaction. *J. Phys. Chem. A* **2009**, *113*, 12961–12971. [CrossRef] [PubMed]
70. Mirzaev, S.S.; Kodirova, N.D.; Nurullaev, M.M.; Khuzhzhiev, M.Y. Study of energy consumption in plasma-chemical dissociation of hydrogen sulfide. *Molod. Uchenyi* **2013**, *2*, 49–52. (In Russian)
71. Startsev, A.N. Low-temperature catalytic decomposition of hydrogen sulfide. *Kinet. Katal.* **2016**, *57*, 516–528. (In Russian) [CrossRef]
72. Startsev, A.N.; Kruglyakova, O.V.; Chesalov Yu, A.; Paukshtis, E.A.; Avdeev, V.I.; Ruzankin, S.P.; Zhdanov, A.A.; Molina, I.Y.; Plyasova, L.M. Low-temperature catalytic decomposition of hydrogen sulfide on metal catalysts under layer of solvent. *J. Sulfur Chem.* **2016**, *37*, 229–240. [CrossRef]

Disclaimer/Publisher's Note: The statements, opinions and data contained in all publications are solely those of the individual author(s) and contributor(s) and not of MDPI and/or the editor(s). MDPI and/or the editor(s) disclaim responsibility for any injury to people or property resulting from any ideas, methods, instructions or products referred to in the content.